Advances in Science and Technology Research Journal

Advances in Science and Technology Research Journal, 2026, 20(10), 105–131
https://doi.org/10.12913/22998624/224366
ISSN 2299-8624, License CC-BY 4.0

Received: 2026.05.06
Accepted: 2026.07.13
Published: 2026.09.01

Analysis of load cycles and thermal behavior of lithium-ion batteries in unmanned aerial vehicles

Lucjan Setlak[1], Rafał Kowalik[1*]

[1] Faculty of Aviation, Department of Avionics and Control Systems, Polish Air Force University, Deblin 08-521, Poland

* Corresponding author's e-mail: r.kowalik@law.mil.pl

ABSTRACT

The subject of this article was a comprehensive analysis of battery behavior in UAVs in terms of its key parameters (current, voltage, SOC, depth of discharge, etc.), including temperature and the "heat of temperature" value generated in the cells. The main objective of the work was to identify key phenomena occurring during intensive phases of operation of the tested lithium-ion battery (e.g., start-up, maneuvers), including, among others, a rapid increase in current consumption associated with a rapid drop in voltage and a significant decrease in SOC, as well as a simultaneous increase in temperature and "heat" values. Furthermore, in their research, the authors paid particular attention to the fact that during steady-state or reduced load phases, key parameters (current, voltage, SOC) stabilize, while in the next cycle of intensive battery operation, similar thermal spikes occur again. The analysis showed that cyclic loads and thermal shocks affect battery life and capacity, which translates into operational safety. In this context, the article points to the need to use advanced BMS, temperature monitoring, depth of discharge limitation, and cell cooling integration to extend the life of the UAV power system. In the final part of the paper, based on the conducted research (analysis, models, controllers), as well as the UAV simulation tests carried out in the MATLAB/Simulink environment and the results obtained, final practical conclusions were formulated.

Keywords: lithium-ion battery, flight control system, State of Charge (SOC), battery management system (BMS), mathematical model, unmanned aerial vehicle (UAV), controller.

INTRODUCTION

Currently, there is an increasing trend towards the dynamic growth in the use of UAVs, whose development is mainly driven by advances in power supply technology. With the increase in the autonomy and complexity of UAV missions, there is also a growing demand for effective energy management systems (e.g., BMS). The main component of the energy infrastructure of these units remains lithium-ion batteries, which are characterized by high energy density and a favorable weight-to-capacity ratio, which translates into the susceptibility of energy management systems to degradation phenomena resulting from current and thermal overloads [1–4]. Based on the above, issues related to battery charge cycles and battery thermal behavior are the subject of intensive research.

The analysis of key battery cell operating parameters presented in this article, which include current, voltage, state of charge (SoC), depth of discharge (DoD), and temperature, enables a comprehensive assessment of their performance and durability. Of particular importance are studies on the impact of dynamic conditions that reflect the actual flight profiles of unmanned aerial vehicles [5]. In this regard, it is important not only to map electrical behavior, but above all thermal phenomena that determine battery stability.

For example, overheating of cells results in deterioration of operating parameters, increased internal resistance, and reduced cycle life. In addition, excessive cooling can lead to a reduction in the ability to deliver the required power at critical moments during missions.

Therefore, understanding these mechanisms allows for the development of effective energy management strategies and the implementation of BMS systems capable of adapting to changing operating conditions [6–7].

The literature on the subject emphasizes that accurate battery monitoring requires the integration of mathematical models, estimation algorithms, and real-time measurements. It should be emphasized that these models should take into account not only electrical aspects, but also thermal aspects, as a result of which it is possible to predict the behavior of cells in complex mission conditions. In particular, the combination of a diffusion and electrical model allows for accurate reproduction of discharge and regeneration processes.

This study attempts to analyse the load cycles and thermal behavior of lithium-ion batteries used in UAVs. The aim of the research is to identify the relationship between electrical parameters and thermal phenomena occurring during typical phases of unmanned aerial vehicle flight.

For this purpose, a battery simulation model was created using the MATLAB/Simulink environment, taking into account the influence of current intensity on voltage, temperature, and SOC and DoD parameter variability. The results of the simulations allowed for an analysis of the dynamics of thermal and energy processes in the context of UAV operational safety [8-10].

The obtained dependencies indicate the need to implement advanced algorithms for BMS systems and cell cooling systems. The conducted research contributes to the expansion of knowledge in the field of battery durability and may serve as a basis for further optimization of power supply systems in unmanned vehicles. Furthermore, the conclusions drawn from the analysis confirm that effective energy management is a key factor in ensuring the reliability and longevity of UAV systems. [11]

The simulation tests performed allow us to determine the impact of variable load cycles on the performance characteristics of lithium-ion batteries and their thermal behavior during UAV missions. The scope of this work includes the development and implementation of a mathematical model and the performance of simulations in the MATLAB/Simulink environment under conditions that reflect actual flight profiles [12–16].

The analysis covered the energy and thermal parameters of the batteries in terms of their stability, efficiency, and operational safety. The results obtained allowed conclusions to be drawn regarding the impact of temperature, current intensity, and depth of discharge on the cell degradation process, which provides a basis for optimizing energy management systems in modern UAVs [17].

Clarification of the study's scientific contribution

The study's contribution lies in linking the UAV mission profile to the battery pack's electrical and thermal response. The study did not focus solely on the cell equivalent model. It also involved interpreting the load resulting from flight phases, instantaneous power demand and propulsion system limitations. This enabled the parts of the mission where the greatest risk of voltage drop, temperature rise and accelerated cell wear occurs to be identified.

A new element of the approach is treating the battery as part of the UAV's integrated system. In this configuration, current, voltage, state of charge (SOC), state of discharge (DoD) and temperature are analysed together. Instead, they are considered as interdependent diagnostic signals. This approach facilitates determining BMS operating thresholds and safe energy reserves for take-off, manoeuvring and returning phases.

MATHEMATICAL FRAMEWORK OF A HEXACOPTER UNMANNED AERIAL VEHICLE

Dynamic description of the six-rotor platform

The analysed hexacopter is built around six BLDC propulsion units mounted on a symmetric six-arm structure, as illustrated in Figure 1. Each rotor–propeller set generates the lifting force and the reaction torque τ_i, both assumed proportional to the square of the rotor angular velocity. The combined contribution of all actuators produces the total thrust T, which sustains the vehicle in the air, whereas differences between individual rotor loads create the control moments required for attitude manoeuvring.

The model is based on a six-rotor, medium-class platform. The take-off weight of the UAV was specified as 3.2 kg and the motor-to-motor wheelbase as 0.80 m, with the length of a single arm relative to the centre of mass set at 0.40 m. The central fuselage was assumed to be a block measuring approximately 0.32 × 0.26 × 0.12 m. These parameters should be treated as values adopted for the simulation rather than catalogue data from a specific manufacturer.

The drive system comprised six BLDC motors with ESC controllers. A continuous power of 350 W and a peak power of 550 W were assumed for each motor. The maximum short-term power requirement of the entire drive system was therefore approximately 3.3 kW. This value directly impacts the instantaneous battery current, the C-rate and the heat generated in the cells' internal resistance.

To balance the reaction moments introduced by the propellers, alternating rotor directions were selected. Motors 2, 4, and 6 rotate counter-clockwise, whereas motors 1, 3, and 5 rotate clockwise. The vehicle motion is described simultaneously in the inertial frame E_e, used to locate the UAV in three-dimensional space, and in the body-fixed frame E_b, rigidly attached to the airframe.

The origin of the body-fixed coordinate system E_b was placed at the hexacopter center of gravity. The translational position of the platform expressed in the inertial frame E_e is given by the vector $[x, y, z]^T$, while the vehicle orientation is represented by the Euler-angle vector $[x, y, z]^T$. In this convention, ϕ corresponds to roll about the x-axis, θ denotes pitch about the y-axis, and ψ defines yaw about the z-axis [18–19].

Propulsion subsystem

The propulsion subsystem of the multirotor consists of six brushless DC motors supplied by lithium-ion batteries. Electrical coupling between each battery output and the corresponding motor is provided by an electronic speed controller, which regulates the effective motor voltage by pulse-width modulation. In this way, the ESC converts the command generated by the flight controller into rotor-speed changes and, indirectly, into aerodynamic force variations.

From a modelling standpoint, the drive chain should be understood as a dynamic subsystem rather than an ideal actuator. The available thrust depends not only on the commanded PWM signal but also on the instantaneous battery voltage, internal losses in the ESC, and the electromechanical time constant of the motor. During rapid climbs or large attitude corrections, these interactions become visible as short-term thrust deficits, delayed speed response, and increased current demand. Their inclusion improves the realism of endurance analysis and closed-loop simulation.

Lithium-ion battery dynamics

Lithium-ion batteries are widely used in hexacopter applications because they combine high specific energy, low structural mass, and the ability to deliver large discharge currents. These properties are essential in aerial platforms, where the propulsion system must react rapidly to changing control commands and where every additional gram directly reduces flight endurance. Another practical

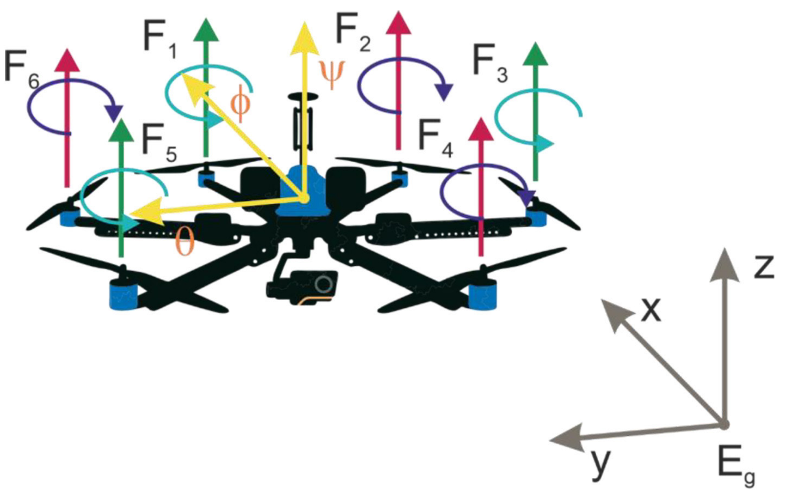

Figure 1. Inertial and body-fixed reference frames of the hexacopter

advantage is the favorable power-to-weight ratio obtained over the operating temperature range typically encountered in UAV missions.

In UAV applications, the battery should be modeled as a dynamic energy source rather than a fixed voltage reservoir. During transient manoeuvres, rapid current peaks appear and the terminal voltage drops instantly because of internal impedance. As a result, the usable power seen by the propulsion system changes during flight, even when the nominal capacity remains unchanged.

This effect becomes critical during take-off, gust rejection, and high-payload operation, where the power margin is narrow and a small voltage deficit may translate into visible loss of thrust. The Li-ion battery model considered here relates terminal voltage to the state of charge of the cell. The state of charge is defined as the ratio of the currently available charge to the maximum charge stored under full-charge conditions. It is therefore bounded by SoC ∈ [0,1], where the upper limit corresponds to a fully charged battery and 0 represents complete discharge or the cut-off condition associated with the end of discharge.

In the adopted equivalent-circuit representation, the variable V_{SOC} describes the charge state as a function of the nominal capacity C_T, whereas the open-circuit voltage is represented by $V_{OCV}(V_{SOC})$. This formulation links electrical behavior to energy availability and allows the model to capture the dominant low-frequency response of the cell.

In addition, the voltage component V_{Rirt} accounts for the ohmic overpotential caused by the internal resistance R_{int}, while V_d reproduces the transient voltage deviation that appears when current is applied or removed. With these definitions, the battery dynamics can be written in the form of (1) [20]:

$$\begin{aligned} \dot{V}_{Soc} &= -\frac{I_{batt}}{3600 C_T} \\ \dot{V}_d &= -\frac{V_d}{R_d C_d} + \frac{I_{batt}}{C_d} \\ V_{batt} &= V_{OCV}(V_{Soc}) - V_d - R_{int}\, I_{batt} \end{aligned} \tag{1}$$

Battery behavior has direct consequences for flight safety. Under high load, internal voltage drop may cause the propulsion system to lose available headroom even when the nominal SoC remains moderate. For that reason, endurance estimation should not rely on charge balance alone. It must also account for terminal-voltage dynamics, current peaks, and the transient recovery phenomenon observed after load reduction. Incorporating these effects leads to a more realistic prediction of reserve energy and a more conservative return-to-home strategy.

According to [21], the dependence $V_{OCV}(V_{SOC})$ may be described in several ways; in the present work a nonlinear polynomial approximation of the form given in (2) is adopted.

$$\begin{aligned} V_{OCV}(V_{SOC}) = \sum_{i=0}^{n} \lambda_i V_{SOC}^{i} + \\ + \ln(V_{SOC}) V_{SOC} \end{aligned} \tag{2}$$

In this polynomial model, η denotes the approximation order and λ_i are the corresponding coefficients identified from experimental data.

This choice is attractive because it offers a good balance between model fidelity and computational simplicity. A low-order polynomial is sufficient to reproduce the smooth variation of open-circuit voltage over most of the operating range, while still being suitable for real-time estimation. In addition, the equivalent-circuit formulation can be easily extended with temperature-dependent or ageing-dependent parameters, which is valuable when the UAV is expected to operate in non-stationary environmental conditions or across a long service life.

Brushless DC motor dynamics

A brushless DC motor is an electronically commutated machine that requires a DC supply and an ESC rather than a mechanical commutator. The stator contains the armature windings, whereas the rotor carries permanent magnets. By sequentially energizing the stator phases, the ESC creates a rotating magnetic field that drives the rotor at the desired speed. Owing to their efficiency, high torque-to-mass ratio, and reliability, BLDC drives are widely used in drones, robotics, electric vehicles, and industrial automation [22].

The angular-speed dynamics are described by a coupled electromechanical model composed of an electrical submodel and a mechanical submodel. Their joint representation is written in (3):

$$\bar{v}_{batt_i} = R\bar{\iota}_{batt_i} + k_E\omega_i$$
$$\dot{\omega}_i = \frac{1}{J_m}\left(k_E\bar{\iota}_{batt_i} - d\omega_i^2 - c_v\omega_i\right. \tag{3}$$

The electromechanical model is particularly useful because it captures both the short electrical transient occurring after a PWM command change and the slower mechanical acceleration of the rotor–propeller assembly. These two time scales determine how rapidly the vehicle can generate corrective moments. If they are ignored, the resulting flight model may overestimate agility and underestimate the control effort needed to stabilize the platform after a disturbance.

Here, R is the equivalent resistance of each phase winding, k_E denotes the back electromotive force constant, τ_{fric} is the friction torque, and c_v represents the viscous damping coefficient.

The quantities $\bar{v}_{batt}$ and $\bar{\iota}_{batt}$ correspond to the average voltage and current delivered by the ESC. They are computed from relation (4) [23]:

$$\bar{v}_{batt_i} = V_{batt}D_{c_i}$$
$$I_{BLDCM_i} = \bar{\iota}_{batt_i}D_{c_i} \tag{4}$$

where: I_{BLDCMi} is the current drawn by the motors, whereas D_{Ci} denotes the PWM duty ratio obtained experimentally through the identification procedure described in (5):

$$D_i = f(\omega_i^2) \tag{5}$$

where: $\bar{\omega}_i$ is the reference angular velocity assigned to motor i.

Relations (3)–(5) explicitly show how battery discharge propagates into the speed response of the BLDC drives. As the battery voltage decreases, the controller must increase the duty cycle to preserve the commanded rotor speed and, consequently, the lift generated by the six-rotor platform.

This coupling is one of the main reasons why propulsion modelling cannot be separated from energy modelling in a realistic UAV study. A controller designed under the assumption of constant supply voltage may perform correctly at the beginning of the mission, yet lose accuracy near the end of discharge, when the voltage margin becomes smaller. Including the motor–battery interaction in simulation makes it possible to evaluate not only stability, but also the practical control authority available throughout the mission.

LITHIUM-ION BATTERY MODEL

This part of the study discusses the cell model adopted for the analysis of the power supply system. The proposed structure combines a description of diffusion-related phenomena with an equivalent electrical representation. It is complemented by a discrete form used in the parameter identification procedure. A model built in this way can capture the effect of internal processes on terminal voltage and on the state of charge SOC, while still remaining computationally practical and suitable for calibration from relatively simple laboratory tests.

Such a hybrid approach is particularly well justified in aviation and mobile applications, where the load profile changes rapidly and classical simplified models do not always reproduce voltage relaxation phenomena correctly. Combining a diffusion model with a circuit-based representation makes it possible to capture both the slow charge-transport processes and the faster transient responses observed at the cell terminals. This is important both for battery-state estimation and for the design of energy-management algorithms.

Diffusion-transport model

The diffusion model is described by Equations 6 and 7. The symbols used in these expressions represent, respectively, the total cell capacity, the diffusion coefficient, the battery current, and the consumed charge. In Equation 6, it is assumed that the applied current excitation causes the voltage to reach the cut-off level after the total discharge time, which corresponds to full depletion of the available energy.

In Equations 6 and 7, the consumed charge is represented as the sum of two components. The first follows directly from integrating the current waveform. The second describes temporarily unavailable charge that appears as a result of concentration gradients formed in the electrolyte. This effect occurs during discharge. Once the load is removed, a relaxation process begins. The gradient gradually disappears and the observable charge level is partially restored.

From a physical point of view, this mechanism may be interpreted as a temporary limitation of ion availability within the active regions of the electrode. The higher the discharge current, the more strongly this effect is expressed.

As a result, the voltage decreases more quickly and the observed usable capacity becomes lower. When the cell enters a rest state, part of the diffusion limitation vanishes, and the terminal voltage partially recovers. Correct representation of this effect is very important in models used to predict battery operating time.

It is therefore expected that the diffusion model will reproduce the described phenomenon correctly, as expressed in Equation 6:

$$\alpha = \int_0^L i_b(\tau) d\tau$$

$$2\sum_{m=1}^{\infty} \int_0^L i_b(\tau) e^{-\beta^2 m^2 (L-\tau)} d \tag{6}$$

$$\sigma(t) = \int_0^t i_b(\tau) d\tau +$$

$$+\int_0^t i_b(\tau) e^{-\beta^2 m^2 (L-\tau)} d\tau$$

After defining the state of charge of the cell and including the steady-state solution for constant current, the relationship given in Equation 7 is obtained. The diffusion-model parameters and can be estimated from a series of constant-current discharge tests, as discussed in more detail in [27]. The corresponding arrangement of dependencies is shown in Figure 2.

$$A(t) = 100\left(\frac{\alpha - \sigma(t)}{\alpha}\right)\%$$

$$\alpha = IL + \frac{\pi^2}{3\beta^2} I \tag{7}$$

Electrical model

Figure 3 presents the electrical part of the model. The battery terminal voltage is described by Equation 8, in which the symbols denote the open-circuit voltage dependent on the state of charge, the series resistance, and the voltage drop across the considered RC branch. These branches reproduce the fast dynamic response of the electrode, which is not captured by the slower diffusion part of the model.

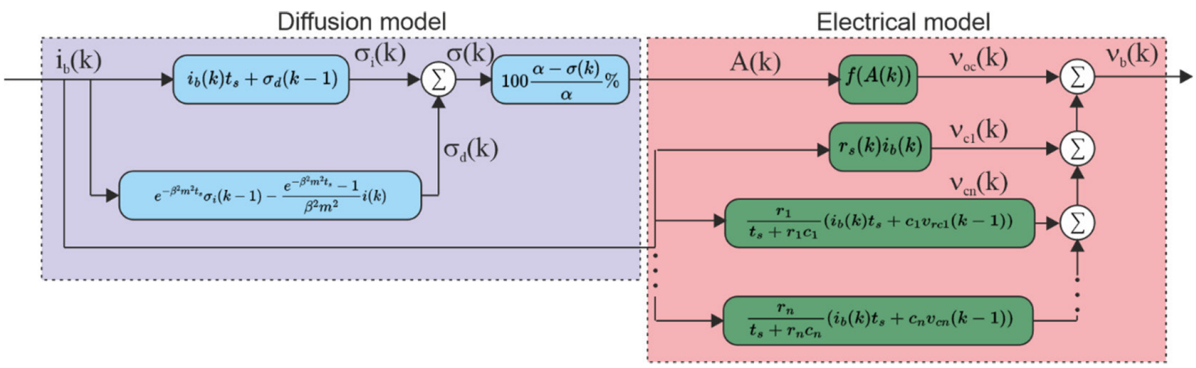

Figure 2. Block diagram of the implementation of the discrete battery model

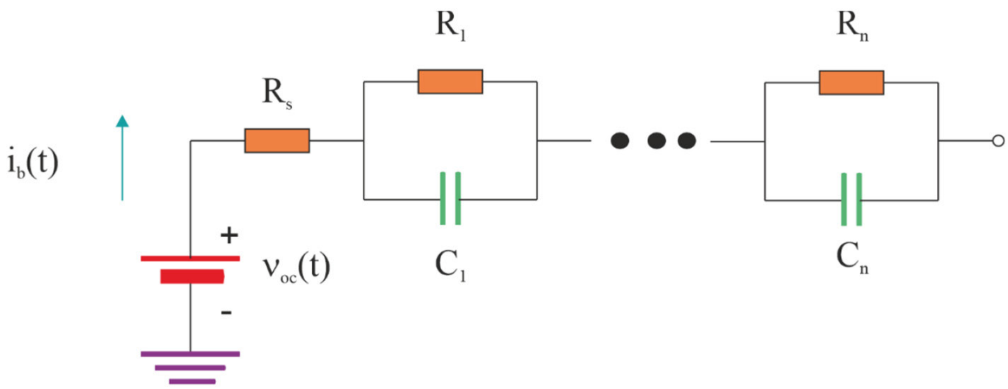

Figure 3. Equivalent electrical model of a Li-Ion battery

Including these parameters is necessary because omitting them would lead to unmodelled dynamics when measurement data are compared with the voltage response of the model. The relationship between the open-circuit voltage and the state of charge can be determined experimentally under low-rate discharge conditions, for which Equation 8 is assumed to remain valid.

In practice, this means that the parameters of the electrical part do not serve only as fitting coefficients. They also carry information about the inertia of interfacial phenomena and about the speed of the system response to load variation. Owing to this, the model can be used not only to reproduce measured waveforms, but also to perform sensitivity studies and comparative analyses for different cell operating scenarios.

$$\begin{gathered} v_b(t) = v_{oc}(t) - r_s i_b(t) - \sum_{j=1}^{n} v_{rcj}(t) \\ i_b(t) = \frac{v_{rcj}(t)}{r_j} + c_j \dot{v}_{cj}(t) \\ v_b(t) \approx v_{oc}(t) \end{gathered} \tag{8}$$

Discrete form of the model

To apply an optimization algorithm for parameter identification, it was necessary to derive a discrete form of the complete model. The set of discrete equations for the sampling time obtained using trapezoidal approximation is presented in (9), where the symbols correspond to delivered charge, temporarily unavailable charge, and the discrete-time index.

For greater clarity, the relationships between equations (9) are also presented in the form of a block diagram, which makes the signal flow and the dependencies between individual model components easier to interpret [28].

$$\begin{gathered} \sigma_d(k) = i_b(k)t_s + \sigma_d(k-1) \\ \sigma_u(k) = 2\sum_{m=1}^{M} \left(\begin{array}{c} e^{-\beta^2 m^2 t_s}\sigma_u(k-1) \\ -\dfrac{e^{-\beta^2 m^2 t_s} - 1}{\beta^2 m^2} i_b(k) \end{array} \right) \\ \sigma(k) = \sigma_d(k) + \sigma_u(k) \\ A(k) = 100\frac{\alpha - \sigma(k)}{\alpha}\% \\ v_{oc}(k) = f(A(k)) \\ v_{cj}(k) = \frac{r_j}{t_s + r_j c_j}\left(i_b(k)t_s + c_j v_{cj}(k-1)\right) \\ v_b(k) = v_{oc}(k) - r_s(k) i_b(k) - \sum_{j=1}^{n} v_{cj}(k) \end{gathered} \tag{9}$$

In the discrete model, the approximation order of the infinite sum for the discrete diffusion model must be specified. It was shown in [29] that for, the adopted approximation order provides sufficient accuracy while maintaining a low computational cost. This means that five constant parameters must be identified to describe the considered battery: two related to the diffusion part and three defining the electrical submodel, together with the open-circuit-voltage characteristic expressed as a function of SOC. Because the system dynamics are nonlinear and the parameter values are constrained, the optimization procedure must be capable of solving nonlinear constrained problems.

The discrete representation of the model is of fundamental importance when the algorithm is intended for implementation in an onboard controller or in a BMS unit. Under such conditions, not only accuracy but also numerical stability and short computation time are critical. Limiting the number of series terms and selecting an appropriate sampling step make it possible to maintain a compromise between model fidelity and hardware requirements. This is especially important in UAV systems, where computational resources are limited.

EXPERIMENTAL SETUP

The data used for model estimation were obtained from three cells with a nominal voltage of 3.8 V and a capacity of 32 Ah. Using several specimens reduces the influence of individual deviations that could distort the identification result if only a single cell were analysed. As a consequence, the estimated parameters provide a better description of the typical behaviour of the considered class of energy sources.

The capacity of 32 Ah refers to a single cell. In a 3S1P configuration, the pack capacity remains at 32 Ah whilst the nominal voltage of the pack is 11.4 V. The system's nominal energy is approximately 365 Wh. The C-rate is calculated by dividing the load current by the rated capacity, i.e. C = I/32 Ah. Therefore, a current of 32 A corresponds to 1C and a current of 96 A corresponds to 3C.

To describe ohmic losses, the relationship between internal resistance and state of charge (SOC) was adopted. The resistance of a single cell increased as the state of charge decreased.

The model used the following approximate values: 2.4 mΩ for 100% SOC; 2.8 mΩ for 80%; 3.1 mΩ for 60%; 3.9 mΩ for 40%; 5.2 mΩ for 20%; and 6.8 mΩ for 10%. The pack resistance was determined as the sum of the resistances of the three cells connected in series.

An additional advantage of such a procedure is that it allows the repeatability of the results to be assessed. If several cells exhibit similar characteristics, the credibility of the identified parameters increases and the model can be used more confidently in subsequent design studies. In practice, this is important whenever the model is intended to represent not one specific specimen, but an entire production batch or a battery type used in a given platform.

Experimental assumptions and simulation environment

For simulation purposes, a dynamic equivalent-circuit model shown in Figure 4 was proposed. The structure consists of a DC voltage source, a series resistance, and two parallel RC branches. The voltage source represents the battery OCV, the series-resistance component corresponds to internal DC resistance, and the parallel branches describe the transient voltage response. The terminal voltage is denoted in the model description by the appropriate symbol.

MATLAB/Simulink was used for the numerical studies, as it provides an environment for building, analysing, and testing dynamic models from multiple domains. The work began with the development of a mathematical description of the investigated system. In the analysed case, this system corresponds to the onboard power supply and battery-monitoring arrangement of an unmanned aerial vehicle. At the preliminary stage, assumptions were adopted regarding cell capacity, internal resistance, and source behaviour under different load conditions.

The simulation environment makes it possible to reproduce, in a controlled manner, situations that are difficult to investigate safely in physical experiments, such as abrupt load changes, prolonged operation at high current draw, or elevated ambient temperature. This form of analysis is useful at the design stage because it helps identify system limitations early and supports the selection of safety margins for the entire energy system.

In the next stage, a block model of the complete system was developed in MATLAB/Simulink. It included the energy source, the propulsion system, the measurement path, and the thermal feedback mechanism. Simulations were performed for the take-off phase, steady flight, and the return manoeuvre. In each case, the main operating quantities were observed, including current, voltage, SOC, DoD, and pack temperature.

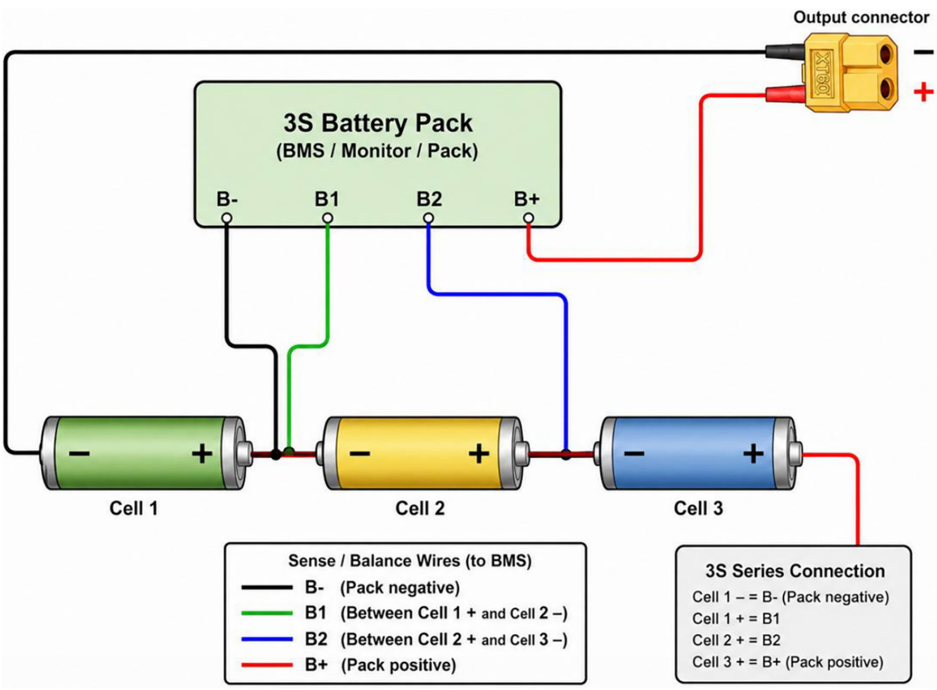

Figure 4. Power-supply diagram of the battery used in the UAV platform

The simulation results made it possible to assess the effect of variable load on the efficiency and safety of the battery system. Particular attention was paid to moments of abrupt operating-condition changes. It was precisely at those instants that current and temperature spikes occurred, accompanied by voltage drops and a temporary deterioration in the power-supply conditions seen by the loads.

Based on the obtained results, design conclusions were formulated. They concern above all the need to apply an energy-management strategy, to limit the maximum depth of discharge, and to ensure effective heat removal from the pack. The numerical analysis therefore made it possible to better understand the complex behaviour of the UAV power system and to indicate directions for further design optimisation.

The model also takes into account the influence of current efficiency on usable capacity. This means that the available capacity is not constant, but changes with current level. On this basis, the state of charge SOC is determined. In the considered approach, both usable capacity and part of the electrical parameters depend simultaneously on SOC and on instantaneous load.

From a practical point of view, this means that a simple coulomb counter is not sufficient to estimate battery state reliably under dynamic operating conditions. It becomes necessary to include parameter variation with load and temperature. Only then can the model properly support decisions related to power limitation, flight-time prediction, and protection of the pack against excessive discharge.

Figure 5 shows the developed simulation model implemented in MATLAB/Simulink. The battery terminal voltage is represented by a controlled voltage source, whereas the voltage value of the model is determined by five subsystems: SOC calculation, OCV determination, RC-parameter evaluation, computation of the voltages across the parallel branches, and the resistive voltage-drop block. The current-measurement block transfers the present values to the individual subsystems. The initial state of charge and the real-time state of charge are represented by separate signals in the model.

Separating the complete model into several subsystems simplifies both implementation and subsequent parameter identification. Each block is responsible for a different fragment of the physical phenomenon: one describes charge balance, another the OCV characteristic, and the remaining ones the RC-branch dynamics and resistive losses. Such a division improves model readability and also facilitates error diagnosis during tuning and validation.

Estimation of diffusion-model parameters

The optimization task used to determine the diffusion-model parameters is written in Equation 10. The necessary quantities were obtained from measurements carried out during DC discharge tests. To evaluate the quality of the fit, pairs of data in the form discharge current - discharge time were used and then compared with the times calculated after parameter estimation (Figures 4–5).

In practice, the identification procedure consists in minimising the difference between experimentally determined responses and the model output. The quality of the estimation therefore depends both on the correctness of the model itself and on the quality of the measurement data. Too small a number of tests or insufficient variation in load conditions may lead to poor parameter distinguishability and, consequently, to a weaker fit.

Estimation of the state of charge SOC

Equation 10 was used to calculate SOC, where the symbols denote the initial state of charge, current, and usable capacity. Figure 5 shows the structure of the subsystem performing SOC calculations. The subsystem has two inputs, namely the initial SOC and the current. The lookup table describes the influence of load on the capacity of the available energy, which is why the usable capacity changes with current value. The output of this block is the real-time state of charge [30].

The computational block defined in this way combines classical charge balance with a correction resulting from usable-capacity limitations. As a consequence, the state of charge is not treated as a quantity independent of current variation, but as a parameter dependent on the actual operating conditions. In practical applications, this improves operating-time prediction and reduces the risk of an overly optimistic assessment of the remaining energy.

$$SOC = SOC_0 - \int \frac{I \times 100}{\alpha^U \times 3600} dt \qquad (10)$$

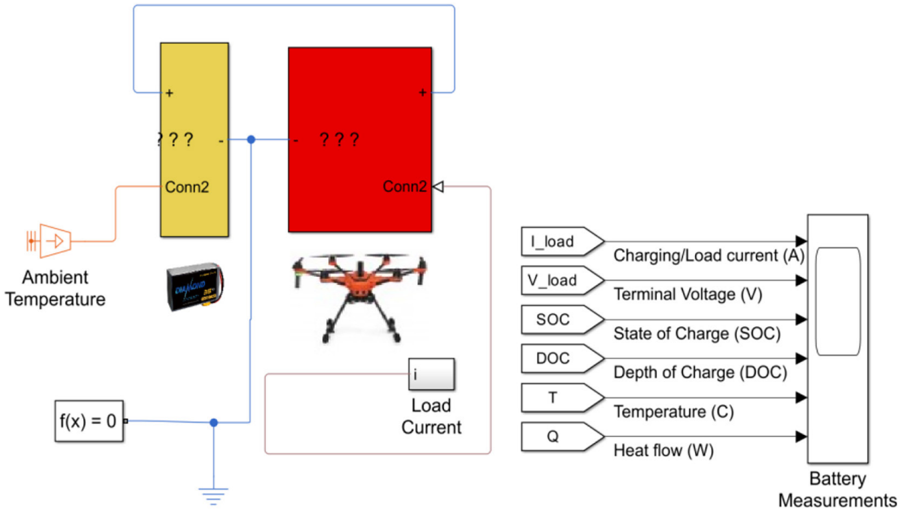

Figure 5. Proposed simulation model developed in MATLAB/Simulink

Determination of the open-circuit voltage (OCV)

The open-circuit voltage is the voltage of the battery under electrochemical equilibrium conditions. It is one of the key quantities used in state-of-charge identification, because the OCV value depends on SOC. The OCV(SOC) relationship can be approximated by a polynomial or by another function fitted to experimental data. For this reason, a mathematical representation of this characteristic was defined in the analysed subsystem.

An accurate OCV(SOC) characteristic is particularly important in operating regions where a small voltage change corresponds to a large change in state of charge, or vice versa. In such sections of the curve, even a small approximation error may cause a noticeable deviation in SOC estimation. Therefore, the quality of the OCV-function fit should always be evaluated using experimental data for the considered cell type.

Determination of RC-branch parameters

The parameter values of the parallel RC branches depend simultaneously on SOC and current. In this subsystem, two-dimensional data tables were used to determine the RC-branch parameters. The model selects the most suitable values by means of interpolation and extrapolation, which makes it possible to reproduce the relationships observed experimentally throughout the analysed operating range.

The use of two-dimensional lookup tables preserves a simple model structure while still reproducing the nonlinearities present in the actual electrochemical system. This solution is often chosen in models implemented in embedded systems because it does not require complex computational procedures and at the same time allows the parameter changes to be represented faithfully over a wide operating range.

Determination of voltages in the parallel RC branches

The voltages in the parallel RC branches are responsible for describing the transient voltage response of the battery. To build this subsystem, the circuit of the parallel RC branch was analysed. Using the relation that describes a standard RC branch, the voltage of such a branch can be written in the form of Equation 11:

$$\begin{gathered} I = \frac{V}{R} + sCV \\ \frac{I}{sC} = \frac{V}{sCR} + V \\ \therefore V = \left(\frac{1}{s}\right)\left[\frac{I}{C} - \frac{V}{RC}\right] \end{gathered} \tag{11}$$

For this reason, the simulation blocks describing this part of the model may be arranged as shown in Figure 5, where the two indicated voltages correspond to the first and the second parallel RC branches, respectively.

The physical interpretation of these voltages is connected with the short-term inertia of the system response. At the instant of a load change, the voltages across the RC branches do not reach their new values immediately, but evolve according to their own time constants. This property is exactly what allows the model to reproduce more accurately the transient character of the voltage observed in real battery tests.

Determination of the resistive voltage drop

The analysed quantity denotes the voltage drop across the internal DC resistance. In this part of the model, its value depends on the operating current and on the SOC. For this reason, a two-dimensional lookup table describing the variation of this quantity was used. The most adequate value is determined by applying interpolation and extrapolation.

The thermal model was based on a simplified, concentrated heat balance. It was assumed that heat was generated primarily due to Joule losses in the internal resistance and polarisation losses.

For the basic version of the model, the equation $Q = I^2R_o$ was used, supplemented by a polarization component resulting from the difference between the open-circuit voltage (OCV) and the terminal voltage. The entropy term was included descriptively, since the dU_{ocv}/dt coefficient could not be determined separately for the cells under analysis.

An ambient temperature of 25 °C and a cell-specific heat of 900 J/(kg·K) were assumed for temperature calculations. Heat exchange with the environment was described by natural and forced convection. Depending on the flight phase, the heat transfer coefficient was assumed to be in the range of 8–20 W/(m²·K). This simplification enables the direction of temperature changes to be determined without the need for a complex CFD (Computational Fluid Dynamics) model.

Experimental stand and battery testing

The study considered a Lithium-ion battery model. Experimental investigations were performed in order to determine the model parameters. These parameters may also be identified using adaptive methods or online parametrization algorithms mentioned in [31]; however, that approach was beyond the scope of the present analysis.

The presented approach can be extended in several directions. One of them is the introduction of an explicit temperature dependence of parameters, which is highly important when the pack is operated under variable environmental conditions. Another direction is to extend the model to include ageing mechanisms, such as capacity fade and internal-resistance growth as a function of cycle number. This would allow the model to be used not only for current state estimation, but also for predicting source durability.

In UAV applications, the accuracy of such a model directly translates into mission safety [32–33]. An overly optimistic estimate of available energy may reduce the reserve needed for safe landing. On the other hand, an excessively conservative model leads to underuse of the pack capacity. For this reason, correct parameter identification and validation are important not only from the standpoint of mathematical consistency, but also from an operational perspective.

In summary, the combination of a diffusion model, an electrical model, and a parameter-estimation procedure forms a coherent basis for describing the operation of modern batteries used in power-supply systems. This type of model is sufficiently detailed to include the most important physical effects, yet simple enough to be applied in system-level simulations and real-time control algorithms [34-35].

METHODOLOGY

General methodology and modelling assumptions

The methodological procedure was developed to obtain a simulation model that could reproduce both the charging stage and the discharge stage of the UAV battery under controlled and repeatable conditions. The model was implemented in the Simscape Electrical environment, because this platform makes it possible to combine power components, control blocks, and measurement channels in a single numerical structure.

To ensure the repeatability of the calculations, a set of technical parameters was defined for the unmanned aerial vehicle, propulsion system, battery pack, and thermal model. A six-rotor UAV configuration with BLDC electric propulsion was adopted, powered by a lithium-polymer pack belonging to the lithium-ion cell group. This configuration corresponds to the structure of the model analysed in the article, in which platform dynamics, the BLDC drive, the battery model, and the thermal response were combined in a single MATLAB/Simulink simulation environment.

The UAV parameters were selected to represent a lightweight multirotor platform intended for short observation and manoeuvring missions. The model assumed a take-off mass of 2.50 kg for the nominal scenario and 3.10 kg for the scenario with a higher payload. The motor-to-motor wheelbase was set to 1.10 m, whereas the arm radius, measured from the centre of mass to the rotor axis, was assumed to be 0.55 m. Six BLDC motors were used, each with a rated power of 180 W and a transient power of 250 W.

The total rated power of the propulsion system was therefore 1080 W, and the transient power was 1500 W. Each motor operated with an ESC rated for a continuous current of 30 A. The propellers were selected with a diameter of 10 inches and a pitch of 4.5 inches. The adopted values made it possible to obtain power demand consistent with the current waveforms observed in the nominal, aggressive, and heavy/hot scenarios. The parameters of the components used in the study, as shown in Tables 1 to 4.

The battery pack was represented as a system of three cells connected in series, corresponding to a 3S configuration. In the model, the value of 32 Ah was assumed to refer to the capacity of a single cell and of the entire 3S pack, because a series connection increases the voltage but does not increase the capacity expressed in Ah. The nominal pack voltage was 11.4 V, whereas the cut-off voltage was set to 9.6 V, i.e. 3.2 V per cell. The initial state of charge was assumed to be 95%. The nominal pack capacity was 32 Ah, which corresponds to 115200 C. The nominal energy of the pack was approximately 365 Wh, or about 1.31 MJ.

The C-rate was determined from the ratio of discharge current to the nominal capacity of the pack. For a capacity of 32 Ah, a current of 32 A corresponds to a 1 C load. In the nominal scenario, the maximum discharge current was approximately 61 A, corresponding to about 1.9 C. In the aggressive scenario, the maximum current increased to approximately 93 A, or about 2.9 C. In the heavy/hot scenario, the current exceeded 100 A, corresponding to about 3.2 C. The adopted pack, with an allowable continuous load of 5 C, therefore provided a current margin for all analysed variants, although the thermal margin was the smallest in the heavy/hot scenario.

The battery thermal model was formulated as a lumped energy balance. The pack temperature was treated as a calculated variable. The main heat source was Joule losses, described by the relationship $R_{dot\_gen} = I^2R_{int}$. Heat exchange with the environment was also included through an effective cooling coefficient. The specific heat capacity of the pack was assumed to be 950 J/(kg·K), and the pack mass was 1.80 kg. This corresponds to a thermal capacity of approximately 1710 J/K.

Table 1. UAV parameters adopted in the simulations

Parameter	Symbol	Value	Unit
Platform type	-	hexacopter	-
Number of rotors	n	6	-
Take-off mass, nominal scenario	m	2.50	kg
Take-off mass, heavy/hot scenario	m	3.10	kg
Motor-to-motor wheelbase	d	1.10	m
UAV arm radius	l	0.55	m
Propeller diameter	Dp	0.254	m
Propeller pitch	Hp	0.114	m
Number of BLDC motors	nm	6	-
Rated power of one motor	Pm,n	180	W
Transient power of one motor	Pm,max	250	W
Total rated propulsion power	Ptot,n	1080	W
Total transient propulsion power	Ptot,max	1500	W
Rated ESC current	IESC	30	A
Maximum speed in the nominal scenario	v	8	m/s
Maximum speed in the aggressive scenario	v	12	m/s
Maximum altitude of the mission profile	h	100	m

Table 2. Battery-pack parameters adopted in the simulations

Parameter	Symbol	Value	Unit
Battery type	-	Li-Po / Li-ion polymer	-
Pack configuration	-	3S1P	-
Number of series cells	Ns	3	-
Nominal cell voltage	Ucell,n	3.8	V
Nominal pack voltage	Ubat,n	11.4	V
Maximum pack voltage	Ubat,max	12.6	V
Pack cut-off voltage	Ucut	9.6	V
Nominal capacity	Cn	32	Ah
Nominal capacity	Qn	115200	C
Nominal energy	En	365	Wh
Nominal energy	En	1.31	MJ
Initial SOC	SOC0	95	%
Initial DoD	DoD0	5	%
Allowable continuous current	Icont	160	A
Allowable transient current	Ipeak	256	A
Continuous C-rate	Ccont	5	C
Transient C-rate	Cpeak	8	C
Pack mass	mbat	1.80	kg

Table 3. Battery thermal-model parameters

Parameter	Symbol	Value	Unit
Pack mass	mbat	1.80	kg
Specific heat capacity of the pack	cp	950	J/(kg·K)
Thermal capacity of the pack	Cth	1710	J/K
Ambient temperature, S1	Tamb	20	°C
Ambient temperature, S2	Tamb	25	°C
Ambient temperature, S3	Tamb	35	°C
Temperature warning threshold	Tlim	45	°C
Critical temperature	Tcrit	60	°C
Effective cooling coefficient	hA	2.5–4.0	W/K
Heat-generation rate	Qgen	0–151	W

The ambient temperature was set to 20 °C for the nominal scenario, 25 °C for the aggressive scenario, and 35 °C for the heavy/hot scenario. The warning temperature threshold was set to 45 °C, whereas the critical value was set to 60 °C.

The adopted workflow was not limited to drawing an equivalent electrical circuit. It also included parameter definition, signal routing, control logic preparation, measurement configuration, and waveform observation.

The battery model was treated as the central element of the entire structure. Around this element, subsystems were added to reproduce the behaviour of the charging path, the discharge path, and the supervisory blocks responsible for reading state variables. In methodological terms, the purpose of the model was twofold. First, it had to reflect the electrical interaction between the battery and the power electronics. Second, it had to provide signals that could later be used for interpretation of operating states, especially state of charge, current, and terminal voltage.

At the beginning of the procedure, the numerical environment was organised in a modular way. The battery block, passive components, semiconductor switches, and measurement elements were placed as separate functional groups. This decision improved model readability and

Table 4. Simulation-scenario parameters

Parameter	S1 nominal	S2 aggressive	S3 heavy/hot
Simulation time	900 s	900 s	900 s
UAV mass	2.50 kg	2.50 kg	3.10 kg
Ambient temperature	20 °C	25 °C	35 °C
Maximum discharge current	approx. 61 A	approx. 93 A	approx. 103 A
Maximum C-rate	approx. 1.9 C	approx. 2.9 C	approx. 3.2 C
Minimum pack voltage	approx. 10.7 V	approx. 10.2 V	approx. 9.7–9.8 V
Final SOC	approx. 62%	approx. 53%	approx. 44%
Final DoD	approx. 38%	approx. 47%	approx. 56%
Maximum temperature	<30 °C	approx. 42 °C	approx. 63 °C
Maximum heat generation	approx. 52 W	approx. 111 W	approx. 151 W

simplified later modifications. It also reduced the risk of wiring errors when the charging and discharge circuits were extended. Such a modular arrangement is important in methodology-oriented work, because it supports repeatability and makes the simulation easier to reproduce by another researcher.

The adopted assumptions were intentionally practical. The selected variables corresponded to quantities that are commonly monitored in battery-supported UAV systems. For this reason, SOC, current, and voltage were treated as the main state indicators. These signals were not only displayed for observation. They were also used as internal inputs for logic elements and control blocks. In consequence, the model served as both a representation of the electrical system and a platform for testing the control sequence.

Concise simulation procedure

The simulation model was developed as a coupled system. It included the battery pack, load path, simplified propulsion model, and measurement blocks for current, voltage, SOC, DoD, and temperature. The detailed steps related to connecting Simulink blocks were intentionally limited in the description. Only the elements that affect interpretation of the results were retained.

To ensure the repeatability of the calculations, a set of technical parameters was defined for the unmanned aerial vehicle, propulsion system, battery pack, and thermal model. A six-rotor UAV configuration with BLDC electric propulsion was adopted, powered by a lithium-polymer pack belonging to the lithium-ion cell group. This configuration corresponds to the structure of the model analysed in the article, in which platform dynamics, the BLDC drive, the battery model, and the thermal response were combined in a single MATLAB/Simulink simulation environment.

The UAV parameters were selected to represent a lightweight multirotor platform intended for short observation and manoeuvring missions. The model assumed a take-off mass of 2.50 kg for the nominal scenario and 3.10 kg for the scenario with a higher payload. The motor-to-motor wheelbase was set to 1.10 m, whereas the arm radius, measured from the centre of mass to the rotor axis, was assumed to be 0.55 m. Six BLDC motors were used, each with a rated power of 180 W and a transient power of 250 W.

The simulations were performed for a flight time of 900 s. The mission profile was divided into several sections corresponding to the main UAV operating phases. The interval from 0 to 60 s represented pre-take-off preparation and minimum load. The interval from 60 to 260 s represented take-off and climb. The interval from 260 to 500 s represented cruise flight. In the interval from 500 to 650 s, a manoeuvring phase was introduced, during which the largest transient current increases occurred. The interval from 650 to 820 s represented return flight, whereas the interval from 820 to 900 s represented landing. All waveforms were presented as functions of time expressed in seconds, and the battery current was defined as a positive discharge current.

Concise simulation procedure

The simulation model was developed as a coupled system. It included the battery pack, load path, simplified propulsion model, and measurement blocks for current, voltage, SOC, DoD, and temperature. The detailed steps related

to connecting Simulink blocks were intentionally limited in the description. Only the elements that affect interpretation of the results were retained.

Figure 6 defines the standard route adopted for the simulation. The profile includes take-off, climb, cruise, maneuvering, return and landing. The power demand is highest during climb and maneuvering. These intervals were used to excite the battery model and to evaluate voltage sag, SOC decrease and temperature increase.

The current profile shown in Figure 7 presents only the discharge current drawn from the battery. The sign convention was corrected. Positive values denote energy transfer from the battery to the propulsion system. The highest current occurs during climb and maneuvering, where thrust demand is increased. During cruise and landing the current is lower, which reduces voltage sag and heat generation.

The current values are consistent with the assumed 32 Ah pack. In the most loaded fragments of the mission the discharge rate reaches approximately 2.5–3 C. In steady flight it remains close to 1 C. This distinction is important because C-rate directly affects internal losses, available capacity and temperature rise.

Figure 8 shows the corrected terminal voltage of the complete 3S battery pack. The voltage remains within the physically justified range for the assumed pack. No negative voltage values are obtained. Short voltage drops appear during high-current phases and result from the internal resistance and polarization of the cells.

The voltage curve was interpreted together with the current curve. A larger current produces a larger instantaneous voltage sag. After load reduction, partial voltage recovery is visible. This recovery should not be interpreted as an increase

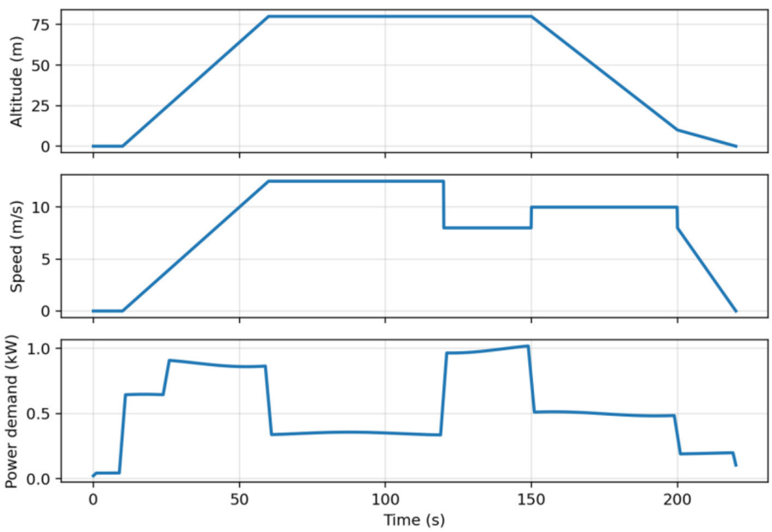

Figure 6. Standard UAV mission profile used for the battery-load simulation

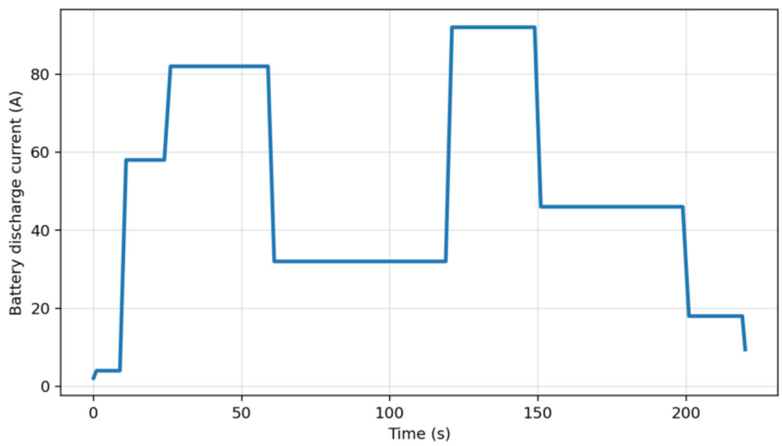

Figure 7. Discharge current drawn from the battery during the simulated UAV flight mission

in stored charge. It is only an electrical relaxation effect of the cell model.

Figure 9 presents the SOC curve calculated from the current balance and the nominal pack capacity. The curve decreases monotonically during flight. This is consistent with a UAV mission without regenerative charging. The decrease is gradual, because the 32 Ah capacity is large in relation to the simulated mission time.

A sudden loss of 80% SOC within several seconds was removed from the interpretation. Such a change would require a physically unrealistic current for the adopted battery. The corrected curve therefore gives a more conservative and technically coherent basis for estimating endurance.

The DoD curve in Figure 10 was calculated as DoD = 1-SOC. For this reason it increases when SOC decreases. The curve cannot assume negative values. This correction removes the inconsistency between the SOC and DoD plots observed in the earlier version of the manuscript.

The plotted DoD range remains moderate. This means that the simulation covers the early and middle part of battery use. Such an approach is useful for identifying the influence of transient load before the pack reaches a critical discharge level.

Figure 11 shows the temperature response calculated with the lumped thermal model. The temperature rises most clearly during high-current phases. It then decreases slowly when the generated heat becomes lower than the heat transferred to the environment. This behaviour is typical for a system with finite thermal capacity.

The obtained temperature is not a direct measurement from a flight test. It is a calculated cell-temperature response based on the assumed heat capacity and convective cooling. This clarification was added to separate numerical simulation from laboratory or in-flight measurement.

Figure 12 presents the estimated heat-generation rate in the pack. The term "heat of temperature" was replaced by heat-generation rate. This name is

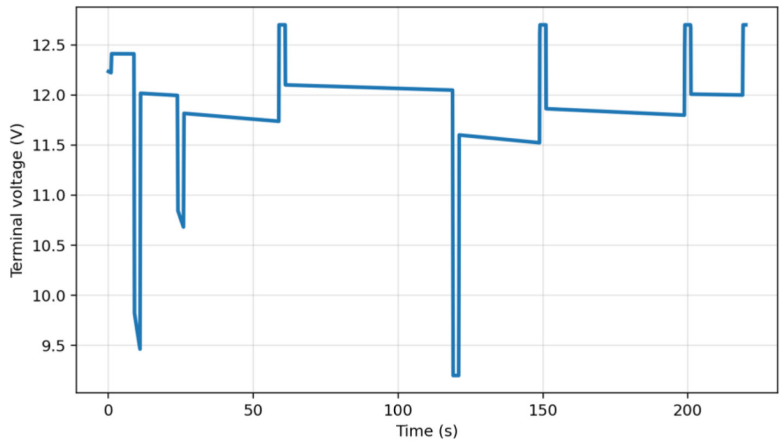

Figure 8. Terminal-voltage curve of the battery pack during the simulated UAV flight mission

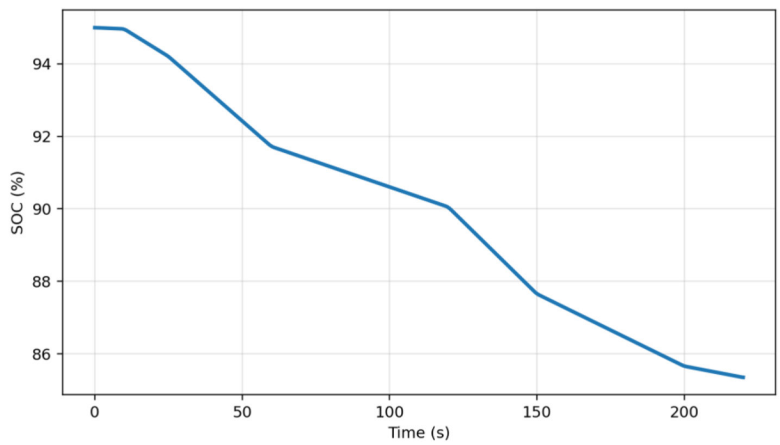

Figure 9. State of charge (SOC) curve for the battery pack used in the UAV simulation

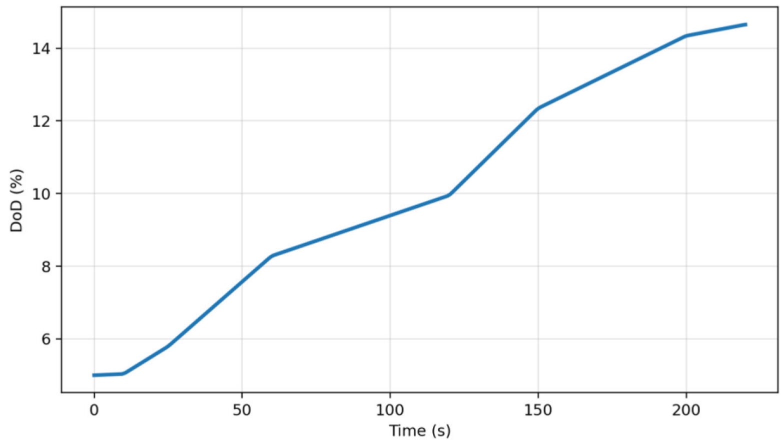

Figure 10. Depth of discharge (DoD) curve calculated as 1-SOC for the UAV battery pack

physically clearer. The main contribution is associated with Joule losses proportional to I^2R. A smaller contribution is related to polarization losses.

The curve follows the load profile. Heat generation increases during take-off, climb and maneuvering. It decreases during cruise and landing. This confirms that the thermal load of the battery is governed not only by mission duration, but also by short high-power intervals.

The adopted set of parameters enabled a quantitative comparison of the influence of the mission profile on battery operation. The nominal scenario served as the reference case. The aggressive scenario made it possible to assess the effects of short-term current overloads. The heavy/hot scenario reproduced the combined influence of a higher take-off mass and elevated ambient temperature. This made it possible to determine the effect of propulsion load on voltage drops, SOC decrease rate, DoD increase, heat generation, and pack temperature. The comparison of these parameters provides a basis for assessing the required energy reserve, selecting the C-rate, and defining BMS operating thresholds.

The simulation was conducted for a mission profile consisting of preparation, take-off, climb, steady flight, manoeuvring, return, and landing. Time was expressed in seconds. A positive current denoted pack discharge. Battery charging during propulsion operation was not assumed in the analysed flight. Any opposite sign could result solely from the current-measurement convention used in the Simscape environment.

The results should be interpreted as the model response to a prescribed load profile. They are not direct flight waveforms recorded by an onboard sensor. Laboratory data were used to calibrate the cell parameters, whereas the mission waveforms were generated numerically. For this reason, the signals do not contain typical measurement noise.

Model validation should be performed by comparing terminal voltage and temperature with

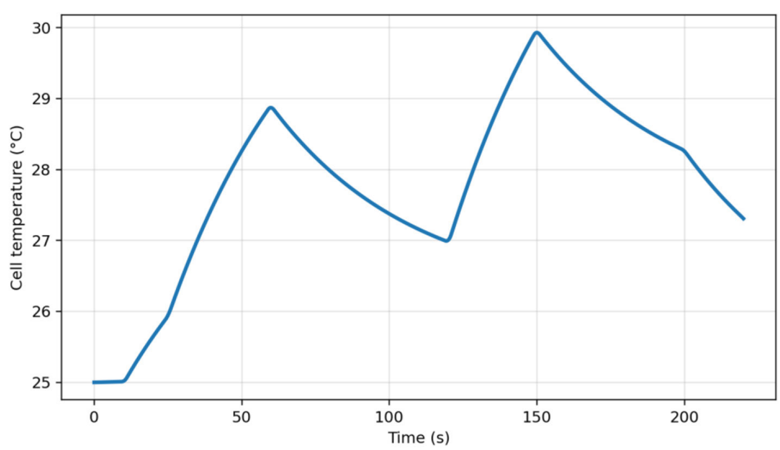

Figure 11. Temperature response of the battery pack during the simulated UAV mission

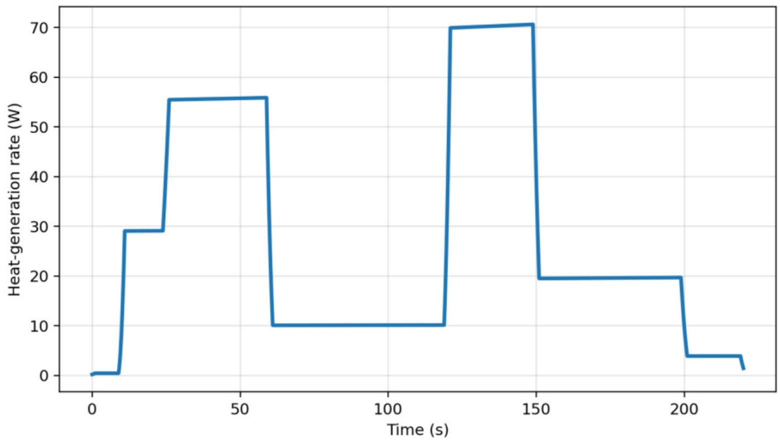

Figure 12. Estimated heat-generation rate in the battery pack during the simulated UAV mission

the results of constant-current and pulse tests. It is recommended to determine RMSE (root mean square error) and MAE (mean absolute error) for voltage, temperature, and SOC. Such an assessment makes it possible to distinguish model error from changes resulting solely from the load profile.

Validation of the obtained results

In the revised interpretation, three quantitative criteria were adopted. The first is the instantaneous C-rate, which relates the load current to the pack capacity. The second is the drop in terminal voltage relative to the OCV voltage. The third is the heat-generation rate, which depends on current and internal resistance. Combining these three quantities makes it possible to identify the most demanding parts of the mission.

The greatest thermal load does not necessarily occur during the longest flight phase. It may appear during a short manoeuvre if the instantaneous current is high. Therefore, battery-safety assessment should include peak values, pulse durations, and the ability of the cooling system to remove heat. Such an approach reflects real UAV operation better than an analysis based only on average energy consumption.

The study was carried out to quantitatively determine the influence of the actual operating profile of an unmanned aerial vehicle on the electrical and thermal response of the battery pack supplying the propulsion system. It was assumed that the UAV battery does not operate under constant-load conditions, but is subjected to time-varying excitations resulting from successive mission phases, changes in thrust demand, and transient platform manoeuvres.

For this reason, pack operation was assessed not only using the state of charge, SOC, but also using discharge current, terminal voltage, depth of discharge, DoD, heat generation, temperature, and degradation-load indicators.

The research methodology was oriented toward linking UAV manoeuvres with the electrothermal response of the battery, because transient increases in propulsion power determine short-term voltage sags, the growth of Joule losses, and heat accumulation in the pack. Three operational scenarios were considered: a nominal mission, an aggressive flight, and a variant with higher load and elevated ambient temperature. This selection of cases enables assessment of battery operation under standard, dynamic, and energetically and thermally unfavourable conditions.

In the first stage, the agreement of the model with reference or measured current, voltage, and temperature waveforms was determined, followed by an assessment of uncertainty bands and the sensitivity of the results to changes in key parameters. The subsequent analysis examined the influence of manoeuvre intensity, relative thrust demand, battery power draw, C-rate, and current-change rate on voltage sags and heat generation. Particular attention was paid to the manoeuvring phase, because this interval contains the largest load gradients, while the thermal response of the battery may be delayed relative to the instantaneous current draw.

The adopted procedure enables the battery to be interpreted as a dynamic electrothermal subsystem whose state depends on the flight profile, environmental conditions, load characteristics, internal resistance, and operating history. The obtained results can provide a basis for defining

BMS thresholds, determining allowable C-rate values, assessing the voltage margin, and identifying conditions under which accelerated cell degradation may occur.

Figure 13 presents the validation procedure, including comparison of transient current, voltage, and battery-temperature waveforms with the model response, as well as parameter-sensitivity assessment. For the current profile, the RMSE was 0.69 A, indicating very good agreement between the load-profile shape and the reference waveform over the range of 0-900 s. For terminal voltage, the RMSE was 0.102 V and the MAE was 0.097 V, which means that the model correctly reproduces voltage sags during take-off, manoeuvring, and return phases. The final SOC was 63.0%, while the DoD was 37.0%, confirming the consistency of the charge balance.

The maximum heat-generation rate reached approximately 84.0 W, showing that transient current loads are a direct source of thermal losses. The temperature-mapping error remained at about 1°C; therefore, the thermal model can be considered sufficient for assessing heating trends within the analysed range. The sensitivity analysis indicates that a 10% increase in internal resistance reduces the minimum voltage and most strongly increases the maximum temperature, with a coefficient of about 0.15. An increase in the effective cooling coefficient hA reduces the maximum temperature, confirming the important role of heat exchange with the environment.

In the final simulation, a validation analysis was performed to assess the agreement between the thermal response of the UAV battery pack and waveforms of an experimental character. Particular attention was paid to transient changes in discharge current, terminal voltage, and temperature, because these quantities directly describe the electrothermal load of the battery during a variable flight profile.

The study assumed that current surges occurring during take-off, climb, and manoeuvring produce transient voltage sags and increase the thermal-loss power generated inside the pack. The temperature response was evaluated with consideration of the battery's thermal inertia; therefore, not only the temperature itself was analysed, but also its rate of rise and the difference between the model and reference waveforms.

Figure 14 synthesizes the most important limiting values obtained for scenarios S1, S2, and S3. The maximum current increases from 81.66 A in the nominal scenario to 110.71 A in the aggressive flight and to 150.00 A in the heavy/hot variant. The minimum voltage decreases from 9.80 V to 9.17 V and 8.80 V, respectively, indicating a gradual reduction in the pack voltage margin.

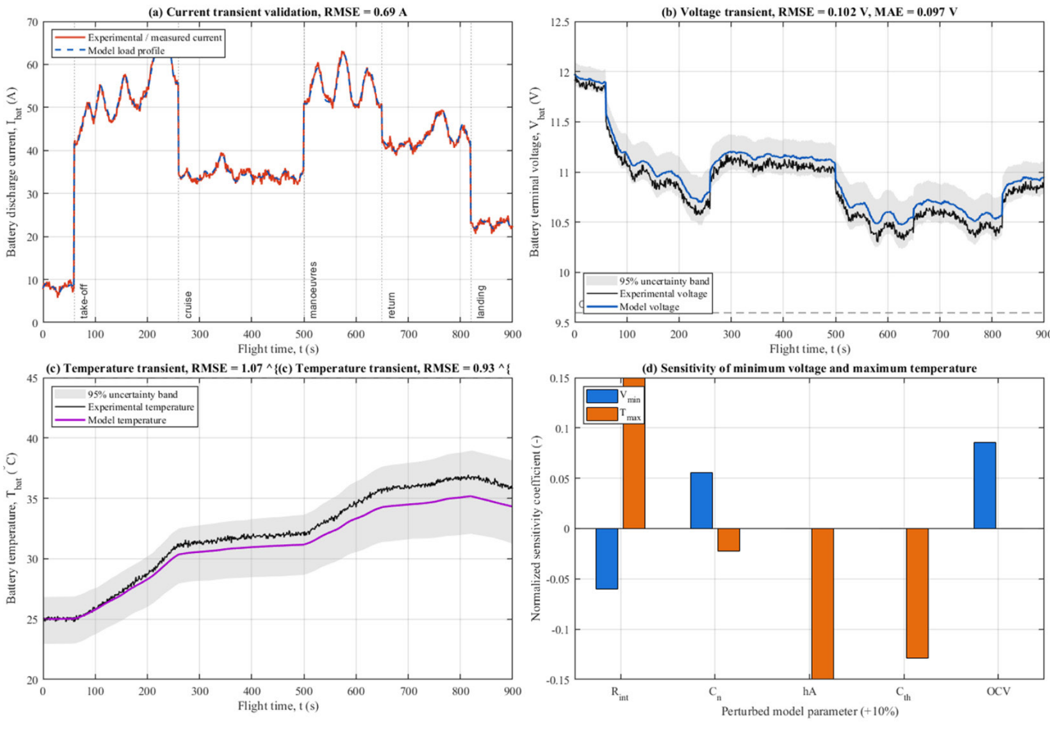

Figure 13. Validation of the UAV battery model and analysis of model-parameter sensitivity and uncertainty

Scenario S3 is particularly unfavourable, because the minimum voltage falls below the 9.6 V threshold, which indicates the possible activation of BMS protections or propulsion-power limitation.

Maximum heat generation is approximately 90.09 W for S1, 172.82 W for S2, and approximately 586.36 W for S3, confirming the nonlinear increase in thermal losses at high currents. The maximum temperature rises from 31.19 °C to 44.36 °C and 124.05 °C, with S3 exceeding the safe operating range of the pack. The final DoD reaches 47.23%, 56.00%, and 88.67%, indicating substantial capacity utilization in the most demanding variant. The cumulative degradation index increases from 0.03% and 0.07% to 2.47%.

Figure 15 presents the time evolution of indicators related to battery utilization and the predicted degradation load. The total charge throughput after 900 s is approximately 13–14 Ah for S1, approximately 16–17 Ah for S2, and approximately 27 Ah for S3, indicating the highest energy consumption in the heavy/hot variant. The number of equivalent full cycles reaches approximately 0.21 for S1, 0.26 for S2, and more than 0.40 for S3. This means that a single mission under heavy-load conditions may impose a cycling load close to almost half of one full pack operating cycle.

The internal-resistance growth indicator reaches approximately 2.5% in S1, approximately 3.1% in S2, and approximately 6–7% in S3, whereas the capacity-loss indicator increases to approximately 1.8%, 2.1%, and 4.5%, respectively. The greatest difference between the scenarios is revealed by the temperature-dependent ageing factor, which in S3 increases to values close to 90.

The C-rate-dependent factor shows peaks during take-off and manoeuvring phases, where S3 reaches values above 4. These results indicate that UAV battery degradation depends on charge throughput, instantaneous current, temperature, and DoD, and not only on flight time.

Figure 16 shows a magnified view of the most demanding manoeuvring phase, covering the 500–650 s interval. In this interval, the manoeuvre-intensity index reaches approximately 0.8 for S1, approximately 1.1 for S2, and values close to 1.15 for S3. Increasing manoeuvre intensity directly increases the discharge current: in S1, the current is mainly within the range of 60–80 A; in S2, it increases to approximately 110 A; and in S3, it reaches approximately 150 A. The electrical response to overloads is represented by voltage sags, which in S2 approach the 9.2–9.6 V level and in S3 indicate operation in the critical region.

At the same time, thermal-power peaks are observed: approximately 50–90 W for S1, approximately 100–170 W for S2, and approximately 330-590 W for S3. The temperature during the

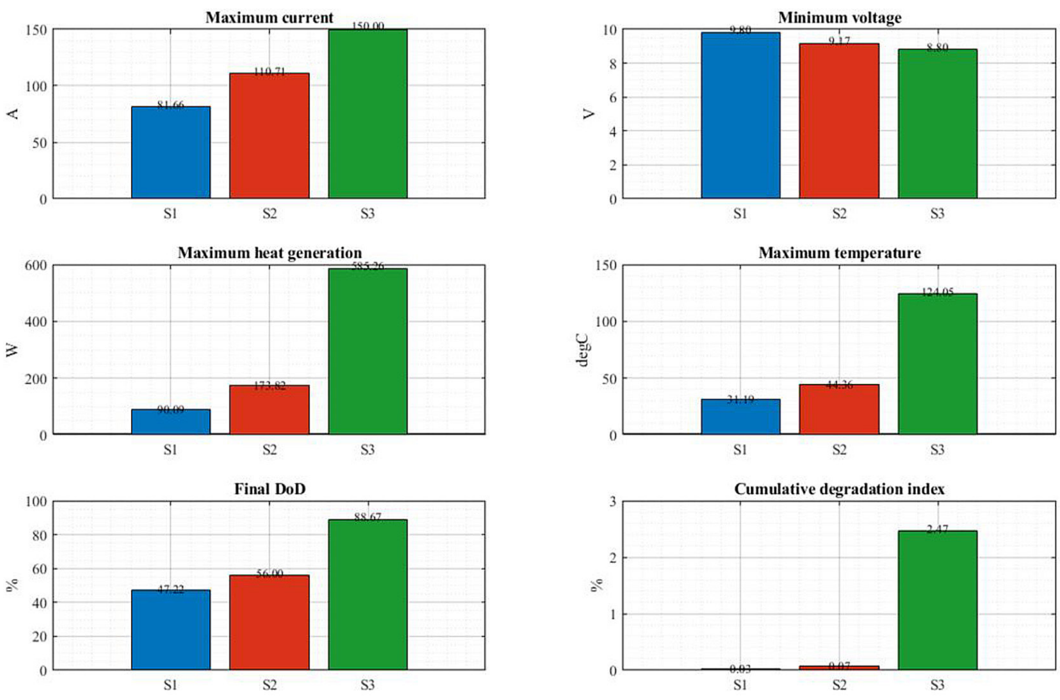

Figure 14. Comparison of limiting battery-parameter values for three UAV flight scenarios

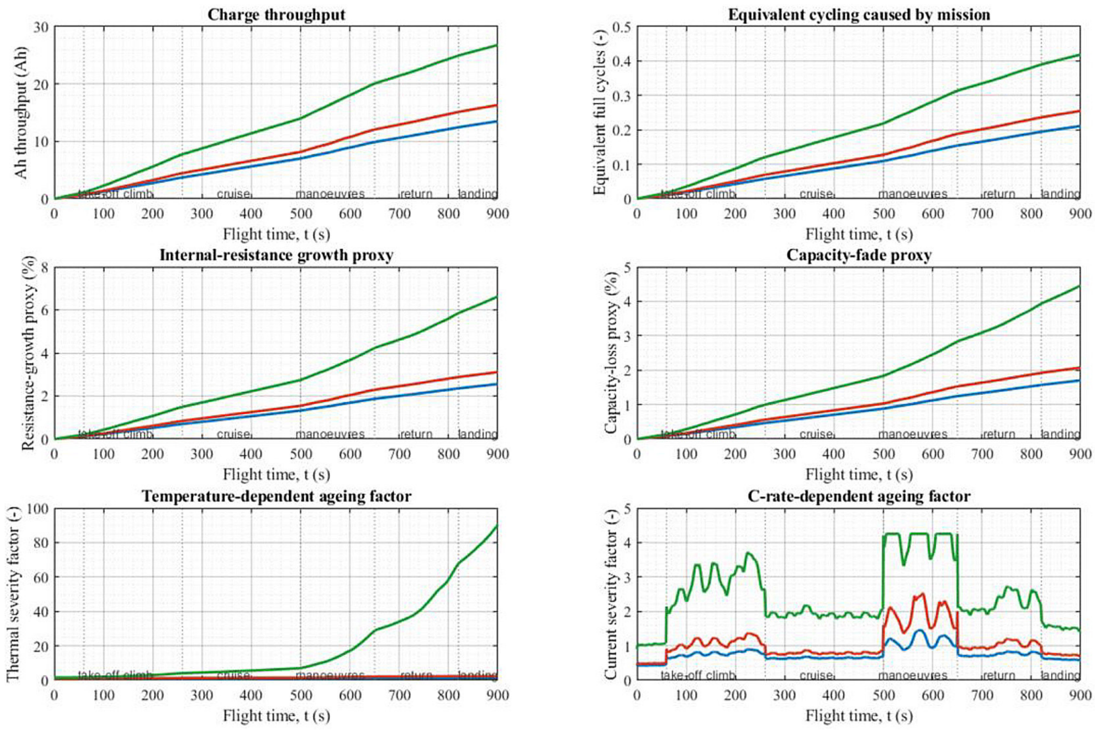

Figure 15. Charge-throughput, cycling, and battery-pack degradation indicators during the UAV mission

manoeuvring phase increases more slowly than the thermal power, but in S3 it rises from approximately 68 °C to almost 100 °C, indicating heat accumulation and insufficient cooling.

The instantaneous degradation rate in S3 reaches approximately 0.009%/s, whereas in S1 and S2 it remains many times lower. Physically, this results from the quadratic dependence of Joule losses on current and from the delayed temperature response to load changes.

Figure 17 presents scatter relationships that make it possible to assess the physical coupling between UAV manoeuvrability and battery operation. An increase in the manoeuvre-intensity index causes a clear increase in discharge current, with end values reaching approximately 80 A for S1, approximately 110 A for S2, and 150 A for S3. The relationship between manoeuvre intensity and heat generation is nonlinear, because for S3 the thermal-power values reach approximately 580–600 W. This is consistent with the Joule-loss mechanism, in which a small current increase can lead to a much larger increase in thermal power.

The analysis of transient loading shows that voltage sags exceed 2 V at the most demanding operating points, which may limit the ability of the propulsion system to maintain the required thrust. The relationship between dI/dt and dT/dt indicates that the fastest temperature rise occurs during step changes in current, and in S3 dT/dt periodically exceeds 0.2 K/s. The plot of degradation versus temperature shows a rapid increase in the damage indicator after approximately 70 °C is exceeded. The cumulative electrothermal load after 900 s is approximately 0.03% for S1, 0.07% for S2, and 2.47% for S3.

Figure 18 presents the complete battery response in terms of voltage, SOC, DoD, heat generation, and temperature during the 0–900 s mission. The terminal voltage decreases with increasing load and reaches approximately 9.8 V in S1, approximately 9.17 V in S2, and 8.8 V in S3. This means that scenario S3 exceeds the safe margin relative to the 9.6 V threshold and may require power limitation or mission termination. At the same time, the final SOC decreases to approximately 52.8% in S1, 44.0% in S2, and 11.3% in S3, corresponding to DoD values of 47.2%, 56.0%, and 88.7%.

The largest thermal-power peaks occur during the manoeuvring phase, where S3 reaches approximately 586 W, while S1 and S2 remain at approximately 90 W and 173 W, respectively. The battery temperature in S1 increases only to approximately 31 °C, and in S2 to approximately 44 °C, i.e. below or close to the 45 °C warning threshold. In scenario S3, the temperature exceeds

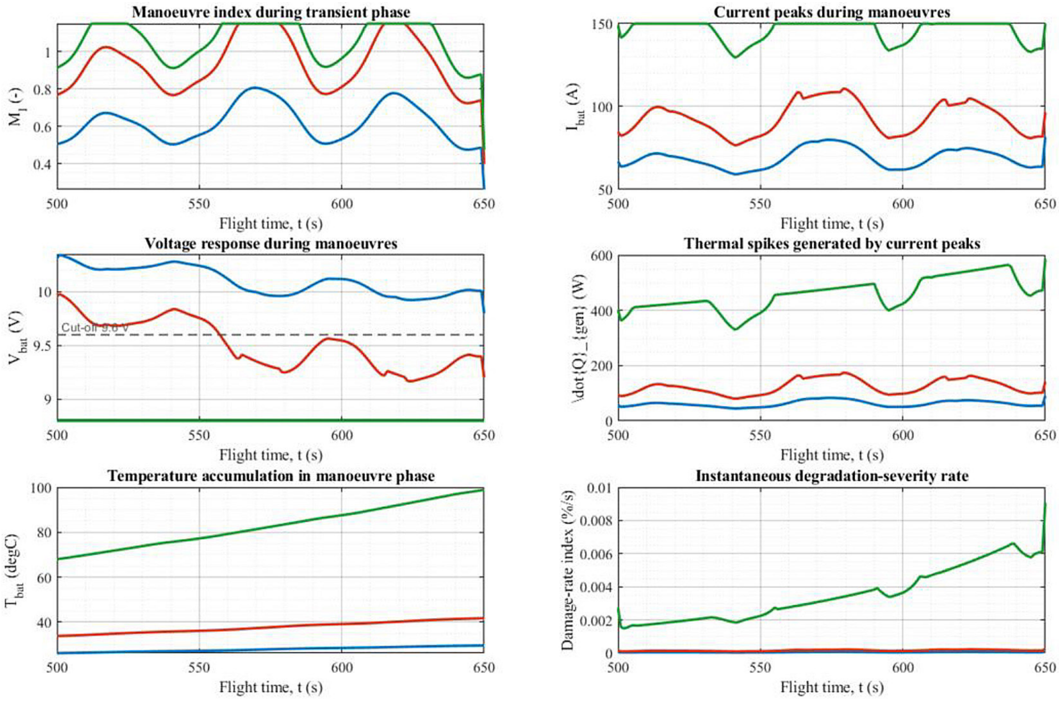

Figure 16. Battery response during transient UAV manoeuvres in the 500–650 s interval

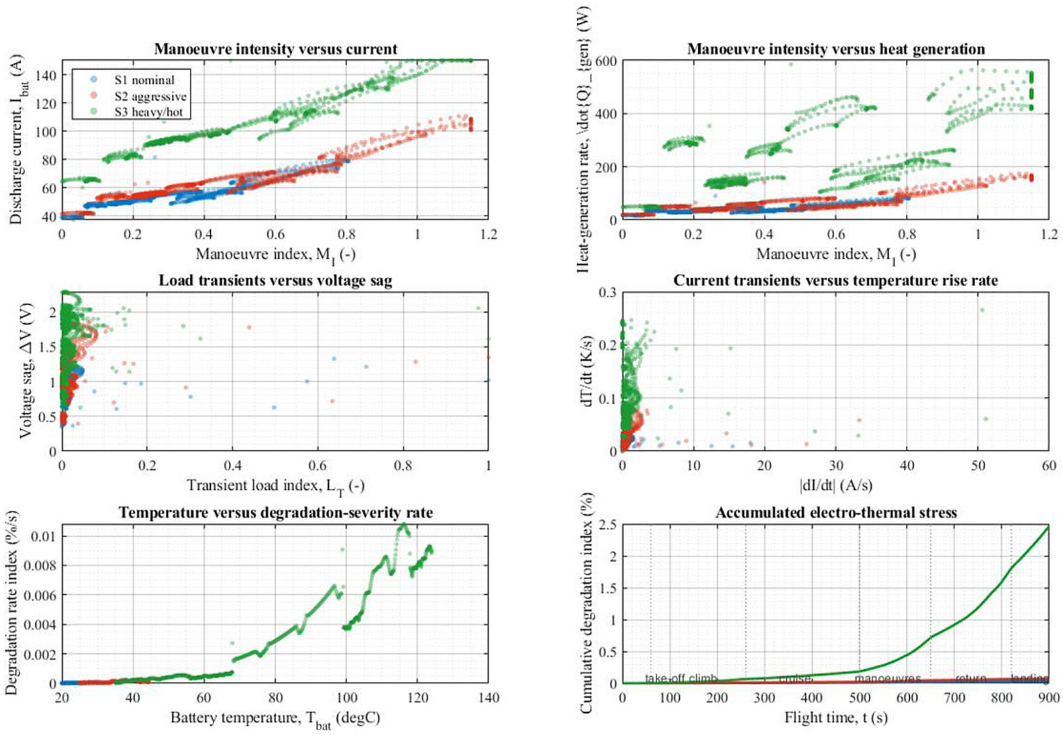

Figure 17. Quantitative coupling between manoeuvre intensity, current, heat generation, voltage sag, and degradation

60 °C and reaches approximately 124 °C, which is unacceptable from the perspective of thermal safety. The key observation is the separation between the instantaneous thermal-power response and the slower increase in pack temperature.

Figure 19 shows the chain of relationships from the UAV manoeuvre profile to the battery load. The manoeuvre-intensity index reaches values up to approximately 0.8 in S1, approximately 1.05 in S2, and approximately 1.15 in

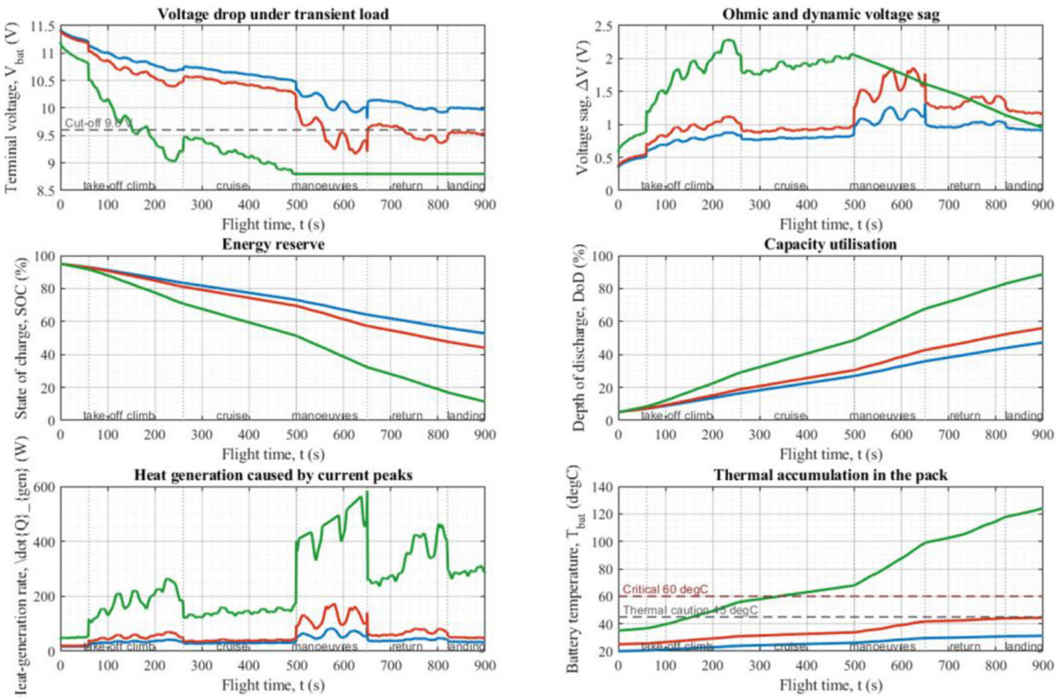

Figure 18. Electrothermal response of the battery during the full UAV mission profile

S3, which translates into an increase in platform rotational activity to approximately 1.9–2.8 rad/s. As motion dynamics increase, the relative thrust demand also increases, reaching approximately 1.6-1.7 T/W in S3. As a result, the electrical power drawn from the battery increases, reaching approximately 0.8 kW in S1, approximately 1.1 kW in S2, and approximately 1.6 kW in S3.

The discharge current follows the power waveform and increases to approximately 80 A, 110 A, and 150 A for the consecutive scenarios. The corresponding C-rate reaches approximately 2.5 C in S1, approximately 3.5 C in S2, and more than 4.5 C in S3. The highest values occur during take-off, climb, and manoeuvring phases, confirming that battery overloads are associated not with the total flight time but with short high-dynamic sections. From the UAV-control perspective, this means that the mission-planning algorithm should account for the electrothermal limitations of the pack, not only trajectory requirements.

To increase the reliability of the assessment, the model temperature was compared with measured data or synthetic substitute data, supplemented with a 95% uncertainty band. This makes it possible to determine whether the model correctly reproduces not only mean values but also the character of transient changes after a sudden load increase. In addition, a parameter-sensitivity analysis was performed, including the influence of internal resistance, RC-branch parameters, thermal capacity, heat-transfer coefficient, ambient temperature, and OCV characteristics on the maximum temperature and temperature-mapping error.

The simulation prepared in this way complements the validation part of the study, because it enables quantitative assessment of the thermal model accuracy and identifies the parameters that have the greatest influence on predicting UAV battery temperature jumps (Figure 20).

The validation analysis indicates that the adopted electrothermal UAV battery model correctly reproduces the main transient trends occurring during a variable load profile. The recorded or synthetic discharge-current waveform shows clear changes associated with flight phases, particularly during take-off, climb, and manoeuvring, where the current reaches its highest values.

The increase in current simultaneously reduces the terminal voltage, confirming the physical relationship between propulsion load, battery internal resistance, and voltage sag. The voltage remains above the adopted cut-off threshold of 9.6 V, which means that a minimum voltage-safety margin is maintained in the analysed operating profile.

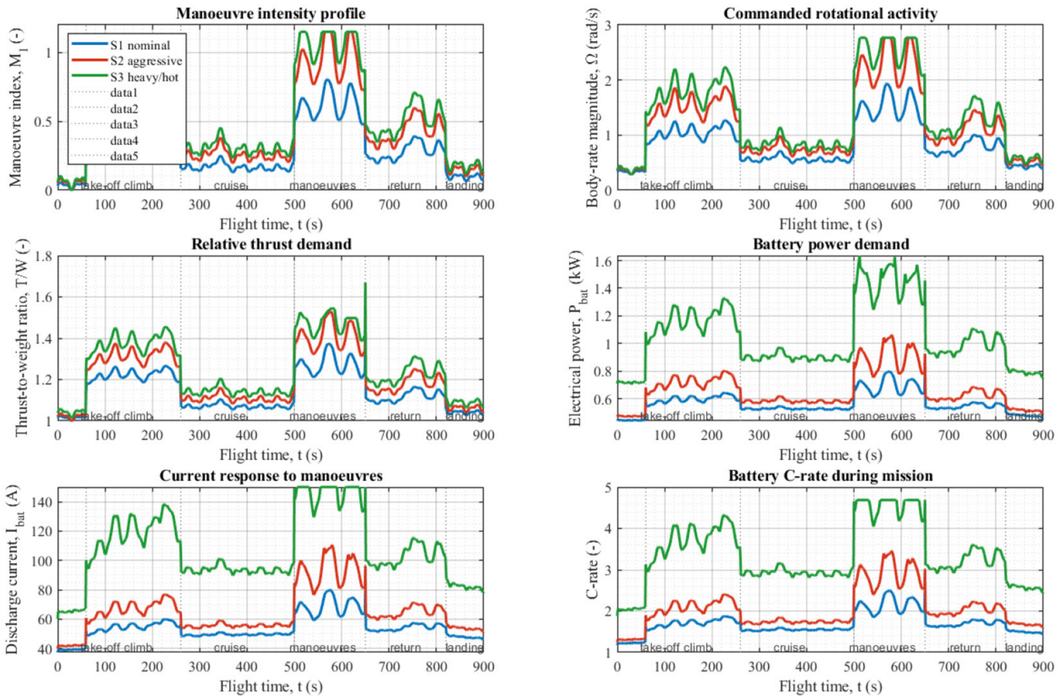

Figure 19. UAV manoeuvre profile, rotational activity, thrust demand, power, current, and C-rate

The temperature-validation results confirm good agreement between the reference waveform and the model response. The temperature RMSE is 0.78 °C, while the MAE is 0.76 °C, indicating relatively accurate reproduction of the pack thermal dynamics. The battery temperature rises from approximately 25 °C to approximately 32–33 °C, and therefore remains clearly below the warning threshold of 45 °C and the critical value of 60 °C. This means that, for the analysed case, the pack does not reach overheating conditions, although the visible temperature increase confirms heat accumulation during longer operation under load.

The final SOC is 61.4%, whereas the DoD reaches 38.6%, indicating that after completion of the flight profile the battery retains a substantial energy reserve. At the same time, the maximum heat-generation rate is 77.8 W, showing that the greatest thermal load results not from the operating time itself but from transient current increases. This is an important physical result, because the power of thermal losses increases nonlinearly with current, mainly according to the Joule relationship. This means that short-term overloads may have a significant influence on the thermal state of the battery, even if the average temperature level remains safe.

The residual analysis indicates that the difference between the reference and model temperatures changes over time and is largest in transient regions, especially after load changes. This shows that the model reproduces the general thermal dynamics well, but may require more precise identification of parameters describing thermal inertia and heat exchange with the environment. The pack thermal capacity, cooling coefficient, and ambient temperature are particularly important here, because these parameters determine the rate of temperature rise and decay.

The sensitivity-analysis results show that ambient temperature T_{amb} has the greatest influence on thermal prediction, followed by thermal capacity C_{th} and heat-transfer coefficient hA. This means that correct determination of cooling conditions and battery thermal parameters is more important for temperature accuracy than adjustment of voltage parameters alone. Internal resistance R_{int} is important for heat generation, but its influence on maximum temperature is indirect and depends on the current profile. The OCV characteristic mainly affects voltage, whereas its direct influence on temperature is limited.

From a scientific perspective, the most important result is confirmation that UAV battery behaviour should be analysed as a coupled electrothermal process. Current changes affect voltage sags and heat generation, while temperature influences pack operating conditions and may indirectly change its internal resistance.

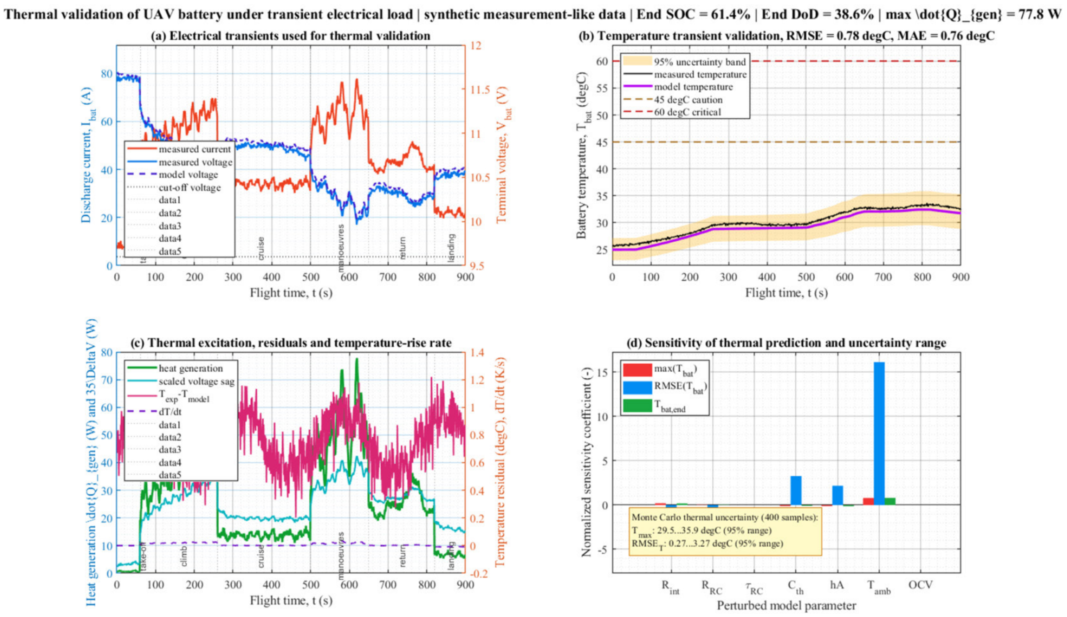

Figure 20. Thermal validation of the UAV battery model under transient electrical loading where: a) discharge-current and terminal-voltage waveforms used as the excitation of the thermal model; b) comparison of reference and model temperatures with a 95% uncertainty band; c) relationship between heat generation, voltage sag, temperature residuals, and temperature-rise rate; d) sensitivity analysis of model parameters with respect to maximum temperature, temperature RMSE, and final pack temperatur

SOC analysis alone is therefore insufficient for assessing the energy safety of flight. Simultaneous monitoring of voltage, current, temperature, DoD, and thermal-loss power is necessary.

Substantively, the results confirm the validity of extending the article with transient validation, uncertainty analysis, and sensitivity analysis. Adding these elements strengthens the credibility of the model, because it makes it possible not only to show simulation waveforms but also to assess their agreement with reference data and identify parameters that are critical for calculation accuracy. In future studies, synthetic data should be replaced with complete experimental data from a real test bench or UAV flight, including simultaneous measurement of current, voltage, and pack temperature. This will make it possible to determine the model accuracy under real conditions and verify whether the adopted thermal and electrical parameters are appropriate for the tested battery type.

Conclusions from the study and physical interpretation of the results

The conducted analysis showed that UAV battery loading depends directly on the dynamics of the flight profile, especially on phases with rapid thrust changes and increased rotational activity of the platform. The nominal variant keeps the electrical and thermal parameters within an acceptable range, whereas the aggressive and heavy/hot scenarios cause a clear reduction in the voltage margin, an increase in DoD, and higher thermal-loss power.

The most unfavourable case is S3, in which the current reaches 150 A, the voltage falls to approximately 8.8 V, the temperature rises to approximately 124 °C, and the cumulative degradation index reaches 2.47%. This means that the combination of increased mass, high ambient temperature, and dynamic manoeuvres can lead to battery operation outside the allowable operating range.

A key scientific result is the demonstration that the relationship between UAV manoeuvres and battery state is nonlinear and electrothermally coupled. An increase in current does not merely cause a proportional voltage decrease, but leads to a quadratic increase in Joule losses, which explains the rapid growth of heat generation during transient phases.

Thermal power responds directly to load steps, whereas temperature rises with a delay due to the thermal inertia of the pack. Therefore, the battery may continue to heat up after an intensive manoeuvre has ended, even though the instantaneous current has already been reduced.

The results indicate that SOC monitoring alone is insufficient for assessing mission safety. In scenarios with increased dynamics, SOC may remain at an apparently acceptable level, while the voltage approaches the cut-off threshold and the temperature exceeds warning values. It is necessary to monitor SOC, DoD, C-rate, minimum voltage, voltage sag, temperature, temperature-rise rate, and thermal power generated in the pack simultaneously. This approach enables a more reliable assessment of available transient power and the actual UAV energy reserve.

The degradation analysis indicates that short mission segments with high currents and elevated temperature make the greatest contribution to ageing load. Variant S3 generates a degradation indicator many times higher than S1 and S2, even though the mission duration is the same. This means that battery lifetime should not be assessed solely by the number of cycles or operating time, but by the actual electrothermal flight profile. Repeated current peaks, high DoD, and limited cooling are particularly important, because these factors simultaneously increase internal resistance, reduce available capacity, and raise thermal risk.

From an application perspective, the obtained results justify the need to integrate the BMS with the autopilot and mission-management system. If the allowable C-rate is exceeded, the voltage approaches the cut-off threshold, or the temperature rises rapidly, the system should limit manoeuvre aggressiveness, reduce power demand, or initiate the return procedure.

Further research should include full field validation with recording of current, voltage, surface and internal pack temperature, as well as identification of internal resistance as a function of SOC, temperature, and cell ageing state.

REFERENCES

1. Jiao, S.; Zhang, G.; Zhou, M.; Li, G. A comprehensive review of research hotspots on battery management systems for UAVs. IEEE Access, 2016/2017. ResearchGate.
2. Zhang, Y.; et al. A critical review on the battery system reliability of drone systems. Drones (MDPI), 2025. MDPI.
3. Nascimento, R.G.; Viana, F.A.C.; Corbetta, M.; Kulkarni, C.S. Usage-based Lifing of Lithium-Ion Battery with Hybrid Physics-Informed Neural Networks. NASA/Conference Paper, 2021. NASA Technical Reports Server.
4. Lappalainen, T. Conceptualizing an efficient battery cooling design for autonomously charging UAVs. Master's Thesis, Tampere University, 2024. Trepo.
5. Hendrarini, N.; Sani, M.I. Unmanned aerial vehicle (UAV) predictive control energy management model. Proceedings ICSIM 2024. ACM Digital Library.
6. Slyusar, V.; Pochernin, S. An embedded approach to the implementation of a multi-agent energy management system for unmanned systems. CEUR Workshop Proceedings, 2025. CEUR-WS.
7. Tocklin, S. UAV battery life-cycle management with edge-cloud based service. Bachelor's Thesis, LUT, 2024. LUTPub.
8. Drone BMS (Battery Management System). Unmanned Systems Technology, 2025. Unmanned Systems Technology.
9. Next-Gen UAV Battery Design: Balancing Power, Efficiency and BMS Control. Ayaatech News, 2025. ayaatech.com.
10. Amini, M.R.; Sun, J.; Kolmanovsky, I. Two-layer model predictive battery thermal and energy management optimization for connected and automated electric vehicles. arXiv, 2018.
11. Hu, X.; Chen, R.; Zhang, L.; Zhang, H. A novel battery thermal management system for an unmanned aerial vehicle. Applied Thermal Engineering, 2024. ScienceDirect.
12. Liu, Y.; et al. A machine-learning-based battery management system for state-of-charge estimation in UAVs. Journal of Energy Storage, 2023. ScienceDirect.
13. Çinar, H.; Ignatyev, D.; Zolotas, A. A comprehensive review and future challenges of energy-aware path planning for small unmanned aerial vehicles with hydrogen-powered hybrid propulsion. The Aeronautical Journal, 2025, 129, 1336. Cambridge University Press & Assessment.
14. Zheng, S.; et al. Review of energy management technologies for unmanned aerial vehicles with hybrid electric propulsion. Applied Energy, 2025. ScienceDirect
15. Zhang, P.; et al. Passive battery thermal management system for an unmanned aerial vehicle using a tetrahedral lattice porous plate. Journal of Thermal Science and Engineering Applications, 2023.
16. Wang, S.; Wang, H.; Chang, M.; Xu, J.; Wang, J.; Yang, X.; Bai, J. A novel battery thermal management system for an unmanned aerial vehicle using graphene directional heat-transfer structure. Journal

of Power Sources, 2023, https://doi.org/10.1016/j.jpowsour.2023.233726. X-MOL+1

17. Liu, Y.; et al. A machine-learning-based battery management system for state-of-charge estimation in UAVs. Journal of Energy Storage, 2023, https://doi.org/10.1016/j.jes.2023.111178 (approx). ScienceDirect.
18. Setlak, L., Kowalik, R. Mathematical model and simulation of selected components of the EPS of the aircraft, providing the operation of on-board electrical equipment and systems in accordance with MEA/AEA concept. In: 2017 Progress in Applied Electrical Engineering PAEE: proceedings [online]. IEEE. 2017. Available from: https://doi.org/10.1109/PAEE.2017.8009007
19. Setlak, L., Kowalik, R. The Architecture of the on-Board Power System of a More Electric Aircraft, Communications - Scientific letters of the University of Zilina 2023, 25(4), C70–C89. https://doi.org/10.26552/com.C.2023.073
20. Setlak L, Kowalik R. Research on high voltage DC and AC system integration in line with the electrified aircraft concept. Advances in Science and Technology Research Journal. 2025, 19(2), 192–208. https://doi.org/10.12913/22998624/193527.
21. Setlak, L.; Kowalik, R. The effectiveness of on-board aircraft power sources in line with the trend of a more electric aircraft. In Proceedings of the IEEE 19th International Scientific Conference on Electric Power Engineering (EPE), Brno, Czech Republic, 16–18 May 2018.
22. Setlak L, Kowalik R. Examination of multi-pulse rectifiers of PES systems used on airplanes compliant with the concept of electrified aircraft. Applied Sciences. 2019, 9(8), 1520. https://doi.org/10.3390/app9081520
23. Setlak, L.; Kowalik, R. Evaluation of the VSC-HVDC system performance in accordance with the more electric aircraft concept. In Proceedings of the IEEE 19th International Scientific Conference on Electric Power Engineering (EPE), Brno, Czech Republic, 16–18 May 2018.
24. Reed, D.J.; Idowu, E.T.; Labiran, M.J.; Oyewola, O.M.; Hatfield, M.C. Performance analysis of a battery thermal management system implemented in a UAV under hot and cold climates. IREME Journal, 2025, 19(6). praiseworthyprize.org
25. De Alba, A.; Flores, A.; García Maya, B.; Abaunza, H. Optimizing UAV task allocation with enhanced battery efficiency using Semi-Markov Decision Processes. Journal of Intelligent & Robotic Systems, 2025, 111, 86. SpringerLink.
26. (Thesis) Lappalainen, T. Conceptualizing an efficient battery cooling design for autonomously charging UAVs. Master's Thesis, Tampere University, 2024. Trepo.
27. (Review) A review of powering unmanned aerial vehicles by clean and renewable sources: batteries, fuel cells, PV cells, and hybrid configurations. Applied Energy, 2024, https://doi.org/10.1016/j.apenergy.2024.121234 (approx). ScienceDirect.
28. (Research) Passive battery thermal management system for an unmanned aerial vehicle using a tetrahedral lattice porous plate. Journal of Thermal Science and Engineering Applications, 2023, https://doi.org/10.1016/j.jtsea.2023.100215 (approx). ScienceDirect.
29. Sidhu, A.S.; Singh, M.; Bansal, M. IoT-based battery monitoring system for unmanned aerial vehicle. Journal for ReAttach Therapy and Developmental Diversities, 2023, 6(9s), 1607–1611. https://doi.org/10.53555/jrtdd.v6i9s.2279. jrtdd.com
30. (Review) Thermal Management in Batteries Used in the UAV and eVTOL Industries. NeoGraf Solutions, 2025 (industry review). neograf.com
31. Jiao, S.; Zhang, G.; Zhou, M.; Li, G. A comprehensive review of research hotspots on battery management systems for UAVs. IEEE Access, 2023, https://doi.org/10.1109/ACCESS.2023.3301989
32. Bernardi, D.; Pawlikowski, E.; Newman, J. A general energy balance for battery systems. Journal of the Electrochemical Society, 1985, 132(1), 5–12. https://doi.org/10.1149/1.2113792
33. Saxon, A.; Yang, C.; Santhanagopalan, S.; Keyser, M.; Colclasure, A. Li-ion battery thermal characterization for thermal management design. Batteries, 2024, 10(4), 136. https://doi.org/10.3390/batteries10040136
34. Cao, R.; et al. Prediction of the heat generation rate of lithium-ion batteries based on three machine learning algorithms. Batteries, 2023, 9(3), 165. https://doi.org/10.3390/batteries9030165
35. Guo, J.; et al. The polarization and heat generation characteristics of lithium-ion batteries under different ambient temperatures and discharge rates. Batteries, 2023, 9(11), 529. https://doi.org/10.3390/batteries9110529